FYS-3931

MASTER'S THESIS IN

SPACE PHYSICS

Review and Test of Funnel Shape Geometries in Solar Wind Acceleration

Robert Trollebø

December 15, 2009

FACULTY OF SCIENCE AND TECHNOLOGY
Department of Physics and Technology
University of Tromsø

Preface

I wish to thank my supervisor, professor Ruth Esser at the University of Tromsø, who has given me many useful advices while working with this master thesis. I am very privileged to have had a supervisor who is an expert in this field of space physics.

I also want to thank my wife, Anastasia, who has been so patient with me during these months, who has encouraged me to study for this degree of master, and who has convinced me deeply about the importance of higher education. I am infinitely thankful for the positive influence Anastasia has affected me by.

Finally, I would like to thank my mom and dad who have always believed in me, and who will now see the result of the work that has kept me so busy in the last months.

- Robert Trollebø,
Tromsø, December 15, 2009

Abstract

The origin and heating of the solar wind is still a puzzle. We review in this study the idea that the solar wind originates in coronal funnels. We place emphasis on the fast solar wind. This study provides primarily a historic overview over the development of the idea of funnel expansion. We present examples of recent solar wind studies that investigate the funnel geometry. These studies include both static and time dependent reconnection geometries. The time dependent reconnection geometry that we present and evaluate in more detail is He et al. [2008]. They present their model in order to explain why blue and red shift of the spectral lines Si II, C IV and Ne VIII can be seen in the same flow tubes on the sun. We have found some of the strengths and weaknesses with this model by comparing the models results to observations and to contemporary papers that treat the same ions. We have found that the model results fit relatively well to observed Doppler shifts (velocities), but that the model ignores the physical mechanism below 5×10^6 m that transports the heavy ions to that height, and it does not fully explain the choices of initial conditions, in particular why the mass input occurs exactly at 5×10^6 m. These challenges with this model may be important to take into account when developing future models of funnels.

Contents

Chapter 1

Introduction: Overview of the Sun and the Solar Wind

The aim of this work is to present an overview of the work done on funnels, and how the knowledge that exists about funnels today has been achieved. Throughout the last 20-30 years the understanding of the flow geometries and physical conditions in the transition region and corona has improved significantly. And new models have superseded old ones as new observational evidences have been uncovered. Before presenting a description of the earliest funnel models (chapter 2), a general introduction about the sun and the solar wind will be given.

1.1 The Sun

The sun is the star at the centre of our solar system. It has a relatively small or medium mass of $M_S = 1.98 \times 10^{30}$ kg, a radius of $R_S = 6.96 \times 10^8$ m, and an age of $\approx 4.6 \times 10^9$ earth years which is approximately half of its expected life time.

The energy from the sun that is incident upon the earth consists primarily of radiation. The spectrum of the radiation from the sun fits rather well to a black body spectrum with a temperature of $T \approx 5.7 \times 10^3$ K (Christensen [2002]), with the inclusion of some absorption lines. The energy in the photosphere ultimately originates in the *core* of the sun, where the temperature is sufficient, $\approx 15 \times 10^6$ K, for nuclear fusion to occur. In the core, hydrogen nuclei (protons) have enough of thermal energy to combine into helium (in a

three-stage process). Excess energy from the nuclear reactions is transported outwards through the *radiation zone*, by photons. In this layer the temperature is already too low for fusion processes. Further out in the interior the temperature decreases to less than $\approx 1 \times 10^6$ K, and some heavy nuclei start to combine with electrons into ions as the electron thermal energy becomes lower than the upper ionisation potential. These transformations make the plasma more opaque. The energy transport by radiation becomes ineffective, and temperature gradients are built up and turbulent convection flows are generated. This layer of the interior is called the *convection zone*. The magnetic field of the sun is generated in this zone. And the characteristic horizontal and vertical flows very much define the magnetic field at the surface of the sun. The *photosphere* is considered to be the surface, because this is where the photons that we see at earth escape from. The photosphere is the layer in which the density has decreased so much that the plasma is no longer opaque. The photosphere contains the temperature minimum of the sun, $\approx 4 \times 10^3$ K (Vernazza et al. [1981]) located approximately 0.5×10^6 m above the photosphere in the chromosphere (see figure 2.1 in chapter 2). Consequently, the gas at this 'cool' temperature layer consists of neutral atoms (hydrogen and helium, mostly).

The convectional flows form distinct features or patterns on the surface, known as *supergranules* ($\approx 30 \times 10^6$ m in size) and above the supergranules a pattern of *granules* ($\approx 1 \times 10^6$ m in size). These granules are the result of the fact that the plasma flows upward and then flows to the sides when it reaches the surface. It then flows downward between the granules in a circular motion. The magnetic field, more or less, follows the flow, resulting in vertical magnetic fields in the borders, and near horizontal field in the centre of the granules and supergranules. The borders are called *lanes*. The lanes on the sun constitute the *network*. The magnetic field in and around lanes and network has a large impact on the magnetic field higher in the solar atmosphere. Both red-shifts and blue-shifts (Doppler shifts) of emission lines have been observed mostly from lanes. And the intensity of certain high temperature lines is higher in lanes than above cells, which indicates that the plasma in lanes is hotter than outside.

Above the photosphere we find the chromosphere, where the temperature increases to approximately $\approx 20 \times 10^3$ K at the top. Here a substantial fraction of helium atoms have been ionised (figure 2.1).

The *corona* is the outer layer of the solar atmosphere. It is a layer which consists mostly of completely ionised elements – plasma, with mostly proton

and electrons. A small fraction of partly ionised heavy elements still exists (known from the emission from these ions). The proton temperature reaches $\approx 2.5 \times 10^6$ (Cranmer et al. [1999]) in the corona, while the electron temperature is slightly lower, $\approx 1 - 1.5 \times 10^6$ (Wilhelm et al. [1998]). The large difference in temperature between the corona and the chromosphere (at least 2 orders of magnitudes) indicates that a region must exist with a large temperature gradient. This region is very thin. It is called the *transition region*. The temperature rises from 2×10^4 K to 1×10^6 K in a layer that is only 100 km thick, and the chromosphere gas transforms into a complete ionised plasma through this layer.

Due to the steep temperature gradient, energy is conducted downward from the hot corona to the cool chromosphere. In the chromosphere this energy is lost by radiation. This energy balance is called 'back heating', and this is explained further in chapter 2.

1.2 The Solar Wind

Ionised gas is flowing away from the sun in all directions. This flux of plasma is called the *solar wind*, and it achieves its velocity in the solar corona. There are two main modes of the solar wind; the fast and the slow solar wind. The fast solar wind originates in coronal holes, which are areas on the sun with open magnetic field lines and low density. The speed of the fast wind is $u \approx 700 - 800 \times 10^3$ ms^{-1} at 1 AU. The density, proton flux density and proton temperature at earth are $n \approx 3 \times 10^6$ m^{-3}, $\phi_p \approx 2 \times 10^{12}$ m^{-2}s^{-1} and $T_p \approx 2.3 \times 10^5$ K, (Lie-Svendsen [2007]). The slow solar wind originates in the vicinity of closed magnetic loops in the so called streamer regions. By the sides, and at the top of these loops, the magnetic field is weaker relative to the magnetic field inside the loops, and the plasma is able to escape along open field lines to the corona where it is further accelerated to the velocity of the slow wind. The speed of the slow wind is on average $u \approx 350 \times 10^3$ ms^{-1}. The other plasma parameters are on average $n \approx 8 \times 10^6$ m^{-3}, $\phi_p \approx 3 \times 10^{12}$ m^{-2}s^{-1} and $T_p \approx 0.3 \times 10^5$ K. If we compare the proton flux density of the fast and slow wind we see that they are approximately the same. The low speed of the slow wind is compensated with high density to maintain the flux density. Both the fast and the slow wind is composed of protons and electrons, some helium ions (5%), and minor numbers of heavier ions such as neon, magnesium and iron. However, the plasma parameters of the slow

wind are very varying. And the helium abundance can reach as high as 20%.

During solar minimum, the holes are usually situated around the poles on the sun (polar coronal holes), although they occasionally extend to lower latitudes. The streamer regions are usually located around the equator. During this period of the solar cycle the slow wind is mostly found to flow outwards in the equator plane of the sun. At solar maximum, however, the situation is more complex. Coronal holes and streamer regions are mixed with active regions, which are constantly changing.

At solar maximum the coronal magnetic field on the sun is not so clearly separated, the magnetic field is much more complex and varying. Both slow and fast wind may appear from anywhere on the sun (Miralles et al. [2004]).

The issue of how the corona is heated to the high temperature that is observed in the corona ($T_p \approx 2.5 \times 10^6$ K) is one that has not fully been understood to this day. But it has been argued by Lie-Svendsen [2007] that this temperature of the corona is a prerequisite for the solar wind; without such an high temperature, there would not have been a solar wind. And the solar wind is an important contribution in the energy loss of the corona. One of the most accepted theories to the high coronal temperature is that the corona is heated by low frequency Alfèn waves. These waves are assumed to be generated low in the solar atmosphere. They propagate upwards, and dissipate energy in protons and heavy ions in the corona.

It has been shown that the geometry of the flux tubes can have significant impact on the solar wind solutions. In the following we investigate the role of funnel geometries. These are flux tubes that expand more rapidly with height than ordinary open coronal holes, and with a much smaller cross section in the lower solar atmosphere. In the following we will present the historic development of the idea of funnel geometries (chapter 2). We will then present examples of static funnel geometry (chapter 3). We then explain the idea of time dependent funnels (chapter 4), by giving two examples, and with emphasis on He et al. [2008]. Finally we give a summary and discussion (chapter 5).

Chapter 2

Development of the Idea of Funnel Geometries

In this chapter a presentation of the history of flux tube geometries will be given, with emphasis on the two main geometries, the one used in the so called standard model and the funnel type introduced by Dowdy et al. [1986]. Many modern static models have been based on this latter model. But an introduction to the standard model is needed as some properties are shared between them.

2.1 The Standard Model

Until the 1980s it was assumed that all magnetic field lines that emerge from the photosphere were connected to the corona (open field lines), but that the field lines were largely constricted to the network lanes (Gabriel [1976]). The field lines were thought to expand rapidly with height from the network lanes through the transition region and lower corona. The reason for such an high magnetic flux concentration in the lanes was due to supergranular convection; the convectional movement pushed the field lines together. The transition region was just the thermal connection between the hot corona and the cool chromosphere. The energy balance in the lower solar atmosphere was composed of two components; heat conduction and radiation. Heat was transferred to the chromosphere by downward heat conduction only (from the hot corona), *back heating*, and the heat was radiated away in the transition region and chromosphere. In addition to downward heat flux, the corona lost

energy in the solar wind. A schematic illustration of this process is shown in figure 2.1. In this figure, the thick line indicates the shape of the magnetic field as it expands out from a network lane. On both sides of the 'neck' in the photosphere, supergranular cells (not marked) constrict the magnetic field into the neck. The plasma parameters in this figure are from Vernazza et al. [1981]. They calculate these parameters from a model of spectral line intensities in close comparison to observations.
The view of the geometry of field lines, and energy balance, as described here has been referred to as the *standard model*.

It was known from observations that the highest intensity transition region emission lines seemed to appear from network lanes. For hotter lines, however, no remarkable difference between emission above network cells and network lanes was seen. The downward heat flux was stronger above lanes because conduction strictly followed magnetic field lines, and because the magnetic field was vertical above the lanes. And a higher intensity was associated with this magnetic flux concentration. In fact, the emission as a function of distance along the surface has been calculated by Gabriel [1976], using three models (model A, model B and model C). Model C (two dimensional network energy balance model) included effects due to supergranular convection, whereas the other models did not. Model C was the only model that predicted the observed increased emission above network lanes. Figure 2.2 shows the field line geometry of the standard model. In this figure, a more thorough illustration of the field line configuration of the standard model is presented. The uniform field lines in the corona all originate in the network lanes, and all the field lines from the photosphere ultimately end up in the corona.

Emission measure. When comparing different models of magnetic geometries with observations, *emission measure* is a useful concept: The abundance of a specific element in a specific temperature interval (or height) in the transition region is manifested by the intensities of the observed spectral line.

The number of quanta produced from an ion species, per cm^3 sec, depends on the density of the ion, n_{ion}, and the collisional excitation rate, C, (Pottasch [1963], Burton et al. [1971], Gabriel [1976]),

$$\int n_{ion} C dr$$

which has the dimension of $[\mathrm{cm}^{-2}\mathrm{s}^{-1}]$. In the above equation, r is the height

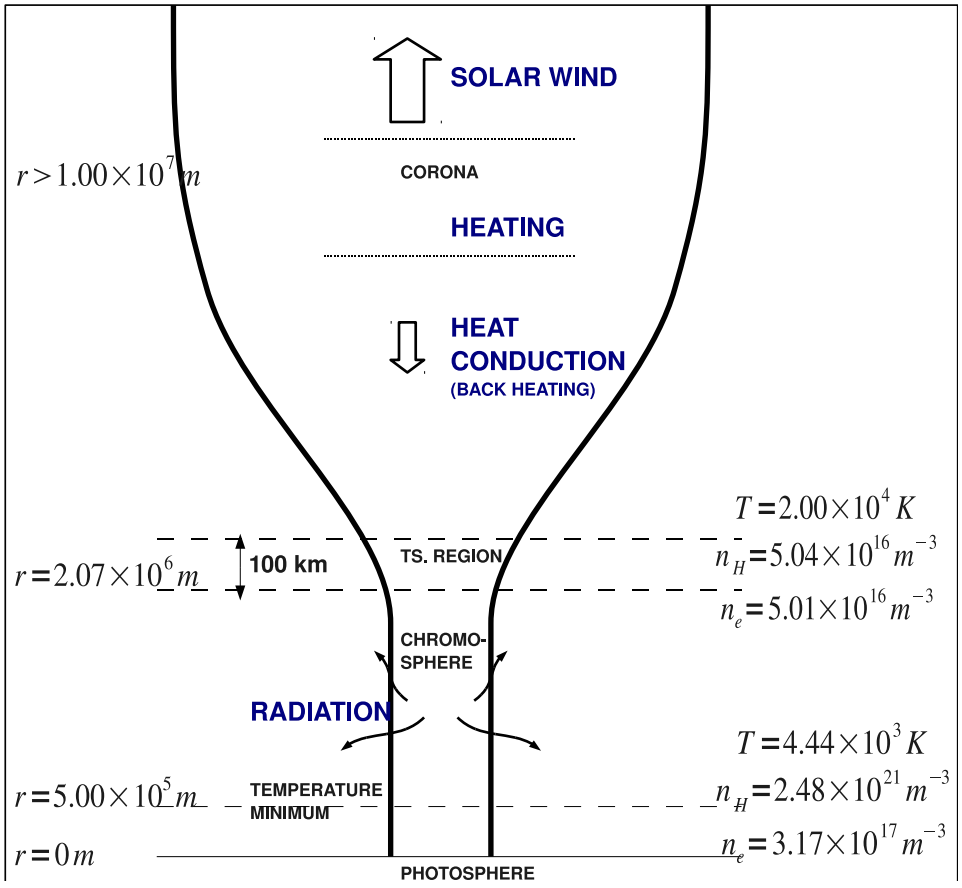

Figure 2.1: **Back heating**: Illustration of back heating. Energy supplied by heat conduction from the corona is lost by radiation in the chromosphere, and the transition region is the thermal connection between the two. The numbers to the left show height above the photosphere. The plasma parameters to the right show temperature, hydrogen density and electron density for the temperature minimum at height $r = 0.5 \times 10^6$ m and at the transition region, and they are from 'model F' in Vernazza et al. [1981]

above the solar limb. The integral extends across the temperature region where the ion exists. Multiplying the last expression with the energy of a quanta, $h\nu$ and 1/2 (while looking perpendicular on the solar surface, only half of radiation is emitted towards the earth), yields the intensity emitted

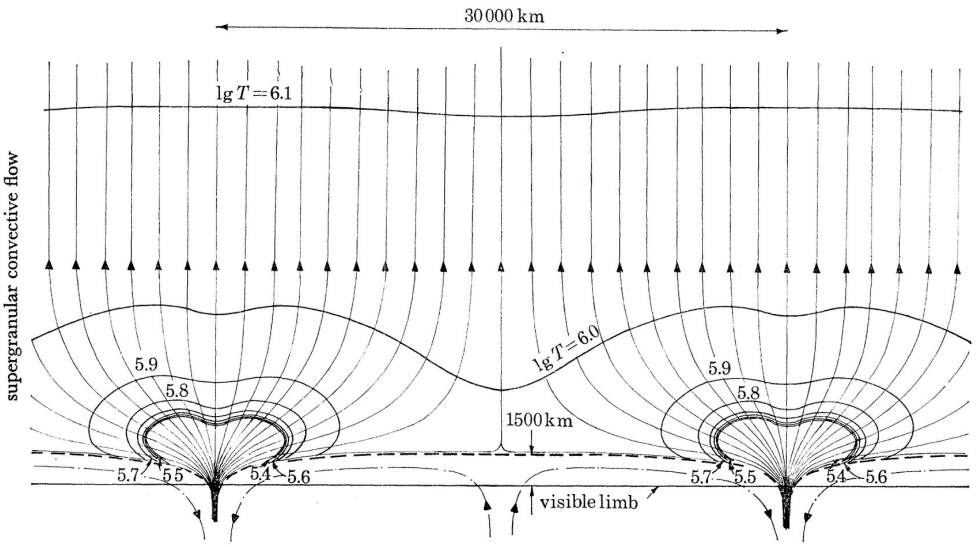

Figure 2.2: **Standard model/model C**: The magnetic field lines (upward arrows) expanding from network lanes, contours of constant temperature (upper solid lines), convective flow (lower solid lines) in the standard model. The transition region is at the accumulative isotherms. As can be seen, the size of the magnetic structures is the same for the super granules (network) — 30000 km. From figure 5 in Gabriel [1976] which is based on 'model C' in the same paper

from the sun ([ergscm^{-2}s^{-1}]),

$$I = \frac{1}{2} h\nu \int n_{ion} C dr$$

Deriving emission measure from observations. It is estimated that the ratio of the density of neutral and ionised hydrogen to electron is $n_H \approx 0.8 n_e$. The above equation can then be written,

$$I \approx 0.8 \frac{1}{2} h\nu \frac{n_{el.}}{n_H} \int \frac{n_{ion}}{n_{el.}} n_e C dr \tag{2.1}$$

where $n_{el.}$ is the elemental density. And it has been assumed that the ratio $n_{el.}/n_H$ does not depend on the height in the transition region. The collisional excitation rate, C, has been defined in the literature to be (Pottasch [1963]),

$$C = 1.7 \times 10^{-3} n_e T^{-1/2} W^{-1} f 10^{-5040 W/T} P(W/kT)$$

in [s^{-1}], where W is the excitation energy [eV], $P(W/kT)$ is a factor that is related to transition probabilities to one state from another (van Regemorter [1962]), and f is oscillator strength (a dimensionless quantity that expresses the strength of a transition, and is proportional to the absorption cross section). If C is inserted into equation (2.1), and then simplifying, we get the result,

$$I \approx 1.1 \times 10^{-15} P f \frac{n_{el.}}{n_H} \int g(T) n_e^2 dr$$

with $g(T) = T^{-1/2} 10^{-5040W/T} (n_{ion}/n_{el.})$ being the *emission function*. For a particular ion, this function has a narrow maximum, and this function thereby reveals the temperature interval in which a particular ion exists. $g(T)$ is normalised by $\langle g(T) \rangle = 0.7\text{Max}(g(T))$. The emission at the distance of earth is achieved by multiplying with $(4/3)\pi(r_{AU}^3/R_S^3)$,

$$I \approx 7.6 \times 10^{-21} P f \langle g(T) \rangle \frac{n_{el.}}{n_H} \int_R n_e^2 dr \tag{2.2}$$

The last expression in equation (2.2), $(n_{el.}/n_H) \int_R n_e^2 dr$, is called the **emission measure** [cm^{-5}], and the integral runs only over the region where $g(T)$ is non-zero, which is the temperature range where the particular ion is formed.

The emission measure is found from observation by measuring the intensity, I, for each line, and computing the function (temperature interval) $\langle g(T) \rangle$ for each line. Since the other variables are known, $n_{el}/n_H \int_R n_e^2 dr$ can be found. For a large number of lines, a set of values on definite temperature intervals are achieved, which are plotted as a function of temperature. An example of observed emission measure is shown in figure (2.3).

The emission measure has been computed for the standard model by for example Athay [1982]. A plot of the computed EM along with observed EM is presented in figure 2.4. As can be seen from this figure, the standard model, such as model C in Gabriel [1976], produces EMs that agree well for temperatures $T > 10^5$ K, but fails to account for the cooler segment $T < 10^5$ K. Although the standard model agrees with many observational features, it is not a satisfactory model especially since it does not explain the emission from the cooler part of the transition region.

During the 1980s as increased resolution improved the magnetograms, it was evident that the photospheric magnetic field was not so uniform and

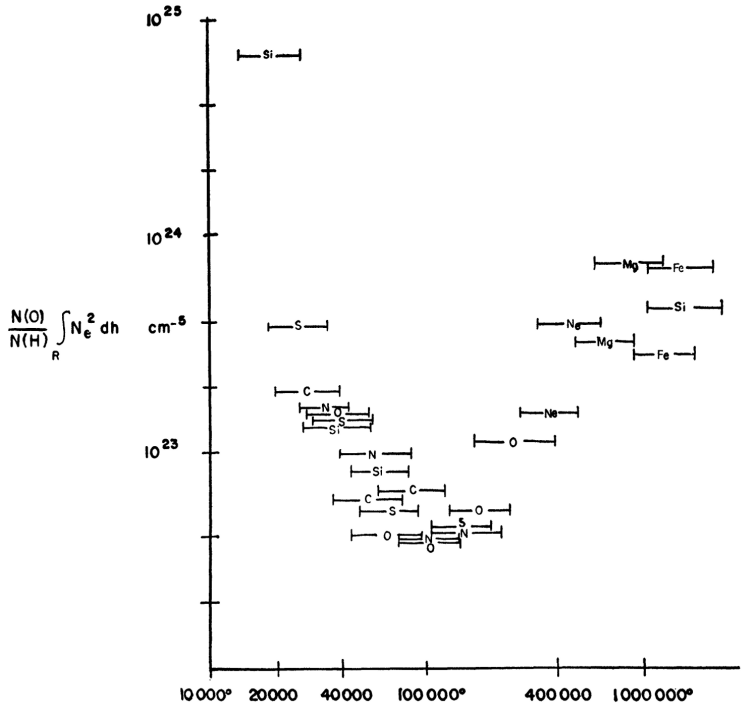

Figure 2.3: Emission measure, computed for many lines. In this figure Pottasch [1963] refer all the abundances to that of oxygen (therefore n_O/n_H instead of n_{el}/n_H). The shape of the curve for n_{el}/n_H would anyway be the same as for this curve. This curve is shifted by the relative abundance between oxygen and the element in question. From Pottasch [1963]

streamlined as seen in figure 2.2. A pattern of fine-scale features were discovered on magnetograms of the photosphere above supergranules and in transition region above network lanes. These fine-scale features consisted of patches of magnetic flux with different magnetic polarities, and they seemed to be concentrated mostly in network lanes. The observations of different polarities radically altered the view on how the magnetic field near the solar surface were arranged. An example of such a magnetogram is presented in figure 2.5 (and 2.7). In this recent magnetogram (of B_z flux) from Hinode we notice that both upward and downward magnetic flux exist (as light and dark patches). If one studies this magnetogram carefully, it is possible to distinguish the network (the centre of supergranular cells has fewer of these

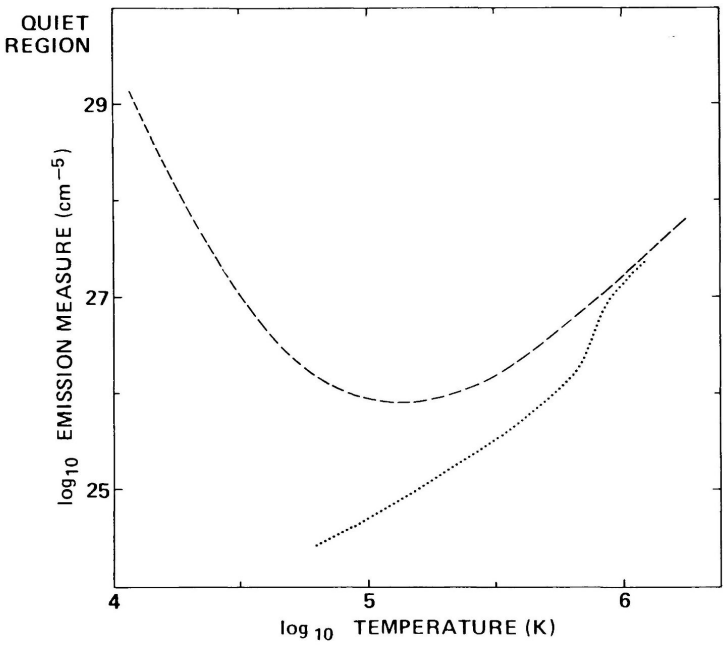

Figure 2.4: **Differential emission measure**: The dashed line is derived from observation. The dotted line is derived from the standard model. It is evident from this figure that such a model does not account for the cooler part of the transition region. From Dowdy et al. [1986] and based on model by Athay [1982]

patches). The standard model did not take into account any such fine scale magnetic features.

Another observation that questioned the standard model was the intensity maps of transition region lines. According to the standard model, the transition region would be very thin because only open field lines were taken into consideration. The emission pattern from the cool transition region ($10^4 < T < 10^5$ K) was expected to be similar to the emission pattern from the hot transition region ($10^5 < T < 10^6$ K). It turned out, however, that the intensity maps of cool lines (of for instance C II) were different than those for hotter lines (such as O VI). The cooler ones showed more bold emission features, than expected, in lanes. And the intensity was very varying along the lane, especially from cool lines.

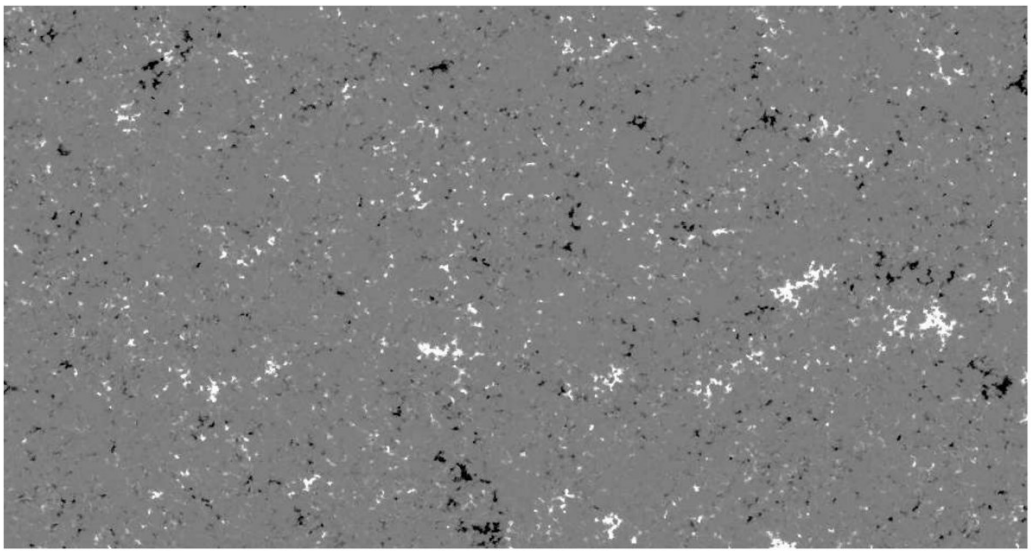

Figure 2.5: **Magnetic polarities**: Hinode SOT/SP magnetogram of a coronal hole at low latitude, recorded November 11 2008. The dimensions are 200×115 [10^6 m]. Light areas are magnetic flux of positive polarity, and dark areas are magnetic flux of negative polarity. The magnetic flux scale is from -500 G to 500 G. From Abramenko et al. [2009]

2.2 The Model By Dowdy et al. [1986]

Based on the observations from magnetograms and intensity maps, Dowdy et al. [1986] suggested an explanation to the shortcoming of the standard model. In the standard model it is automatically assumed that since all field lines in the corona originate in the network lanes, the vice versa is also true (that all field lines in the lanes reach the corona). They argue that this is not necessarily so: Parts of the flux in the network lanes may be foot points of closed loops. Thus it is suggested that the magnetic landscape consists of two components: open *funnels* and closed *loops*. An illustration of this is shown in figure 2.6. Here we see the magnetic picture along a network lane. We see that the funnels (white areas) are intermingled with closed loops (dark areas), and due to this intersection of cool plasma through regions of hot plasma, we may get more emission from cool lines than what is expected in the standard model, and which agree more to the observations. The reason for this two-component magnetic field picture is again the continuous supergranulational

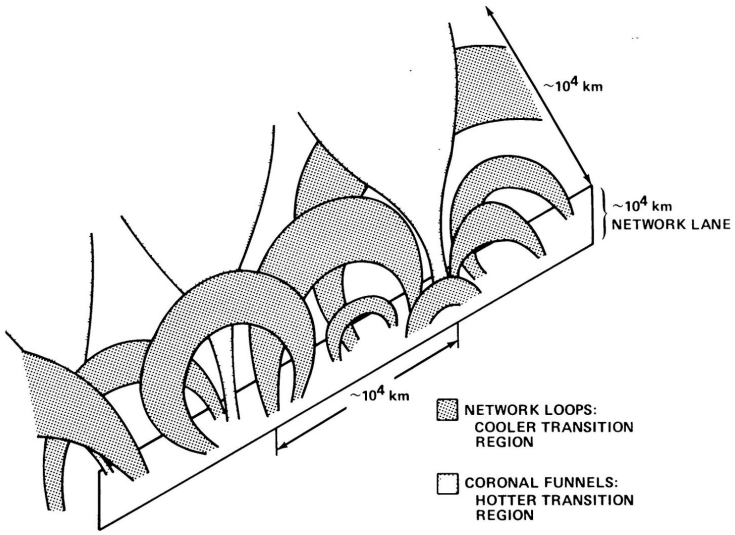

Figure 2.6: **Static model**: A cartoon of the magnetic field according to Dowdy et al. [1986]. Loops are intermingled with funnels and may share the magnetic flux in their foot points with funnels in their neck. The hot branch of the emission originates primarily in the funnel, while the cool branch origin in closed loops. From Dowdy et al. [1986].

flow that is responsible for moving foot points of loops along the lane. The existence of loops in the network lanes explains both why different magnetic polarities are shown in magnetograms, and why emission from cool lines is so bold and structured and why the intensity is so high in network lanes.

The funnels according to Dowdy et al. [1986] are open field lines with much the same geometry as in the standard model, but with even narrower neck. Dowdy et al. [1986] argue that some of the patches of strong flux that we see in figure 2.5 contain the neck of funnels, but the foot point of loops also shares a smaller part of this flux, which is the principal difference between the standard model and Dowdy et al. [1986]'s model. The field strength in these patches can reach up to 500 Gauss. So the cooler transition region is populated with many closed loops that are intermingled with the open funnels. This may also explain why EM of standard models does not fit observational EM for $T < 10^5$ K: Most of the cooler transition region is contained in the loops, and is therefore not energetically connected to the corona. The back heating process is not applicable to the plasma in the loops,

because they are heated internally. The hotter transition region, however, is mostly found in funnels, and the energy is supplied by heat conduction from the corona – back heating, as in the standard model.

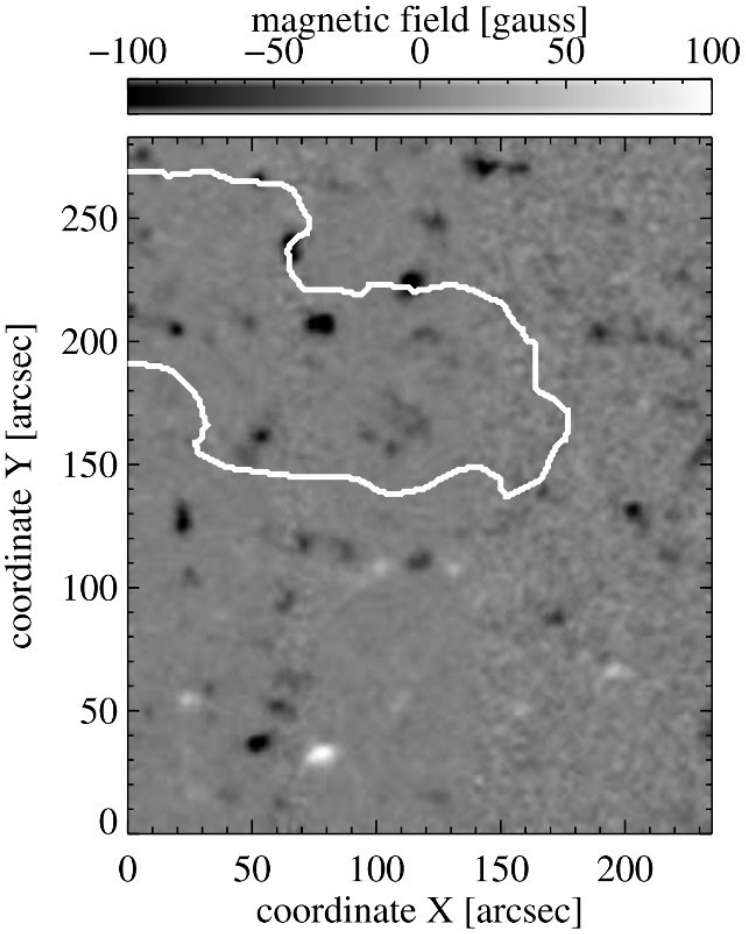

Figure 2.7: **Magnetic polarities**: MDI/SOHO magnetogram recorded on March 7 1997. The area encircled by a white line is a coronal hole. Outside is an quiet sun area. The scale on the top defines the magnetic field strength (light areas are magnetic flux of positive polarity, and dark areas are magnetic flux of negative polarity). From Aiouaz [2008]

Chapter 3

Examples of Static Funnel Models

Based on the ideas by Dowdy et al. [1986] the following expression has been used to describe the geometry of funnels (Janse et al. [2007] and Kopp and Holzer [1976]),

$$A(r) = A_0 \left(\frac{r}{R_S}\right)^2 F_1 \cdot F_2 \tag{3.1}$$

where $A(r)$ is area as a function of heliocentric distance r, and where,

$$F_1 = \frac{f_{m1} e^{(r-r_{g1})/\sigma_{g1}} + f_{g1}}{e^{(r-r_{g1})/\sigma_{g1}} + 1}$$
$$F_2 = \frac{f_{m2} e^{(r-r_{g2})/\sigma_{g2}} + f_{g2}}{e^{(r-r_{g2})/\sigma_{g2}} + 1}$$

The function $A(r)$ describes the degree of expansion relative to radial expansion. The expansion is represented by the functions F_1 and F_2 which determine the inner and outer super-radial expansion, respectively. In the above equations, A_0 is the area of the flux tube at the lower boundary, and R_S is the solar radius. The function f_{g1} is defined as $f_{g1} = 1-(f_{m1}-1)e^{(R_s-r_{g1})/\sigma_{g1}}$ (the function f_{g2} is defined similarly). f_{m1} and f_{m2} specify how many more times the flux tube opens than a radial tube. r_{g1} indicates where the funnel expansion takes place, and r_{g2} where the coronal hole super-radial expansion occurs. And σ_{g1} and σ_{g2} specify over what distance the expansions take place, in the two regions. For an ordinary coronal hole, f_{m1} is in the order

of 5 to 7 and $F_2 = 1$. For a radially expanding solar wind, the functions F_1 and F_2 are $F_1 = F_2 = 1$.

An example with $f_{m2} = 5$ is shown in figure 3.1. The dashed line is for a coronal hole type geometry, and the solid line for a funnel. Each of these geometries in this example has their unique set of expansion parameters. It is clear that the funnel surface area is much smaller than the coronal hole, and that the funnel expands more rapidly than the coronal hole. At a distance of $\sim 1.03 R_S$ the two geometries become similar, because they share the same expansion parameters for the outer segment.

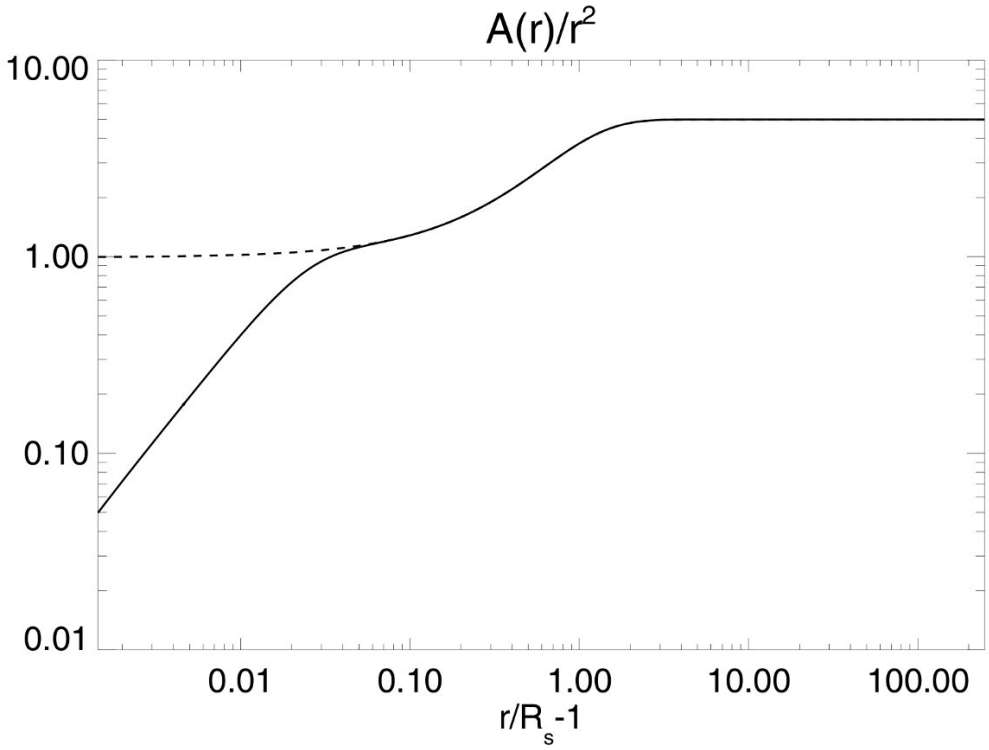

Figure 3.1: **Example of flux tube expansions**: Comparison of two flux tube expansion $A(r)/r^2$ as a function of distance. The dashed line is for a coronal hole, and the solid line is for a funnel (from Janse et al. [2007]).

In the following we will summarise three solar wind model studies that make use of the funnel type expansion. In the examples presented below the solar wind equations for mass, momentum and energy conservation are

solved. The resulting solar wind parameters are in good agreement with observations.

3.1 Esser et al. [2005]

Esser et al. [2005] use a model to show that a large expansion factor of the magnetic field produces results that agree to observations of Ly-α emission in the transition region. The expansion factor can be varied in the model, and it is adjusted to fit the Ly-α observations in the best way. Two set of results are calculated, one with a small expansion factor (traditional coronal hole), and one with a large expansion factor (funnel). The expansion parameters that are used for the funnel are $f_{m1} = 62$ and $f_{m2} = 7$. It is demonstrated that a small expansion factor is unable to account for the Ly-α emission; the emission is only 1/10 of what it should be according to observations. A larger expansion factor agrees much better to observations, both of the Ly-α emission and electron temperature. There are three main reasons for this: Firstly, at a given temperature, downward heat flux density in the corona is smaller in a funnel than in a flow tube that expands less. So the electron temperature can be increased without increasing the mass flux. Secondly, although the heat flux density increases further down in the funnel most of the energy is not converted to radiation but is used to heat the upwelling plasma. And since the particle flux density must be large in the funnel, to sustain the observed mass flux, a large energy flux density is needed. Thirdly, since the hydrogen is brought out of ionisation equilibrium, in this fast flow tube of the funnel, the Ly-α loss take place at a higher temperature where the excitation rate is much higher. A higher excitation rate means that a lower density is needed in order to maintain the same degree of cooling. So in a funnel, the Lyα is much higher than in a geometry with smaller expansion.

As shown in figure 3.2 the energy flux density is plotted as a function of electron temperature for both funnel and hole geometry. In the hole geometry where the hydrogen is close to ionisation equilibrium the Ly-α radiation is small. In the funnel geometry the hydrogen is way out of ionisation equilibrium due to the high outflow velocity. Outflow velocity is higher in the flux tube with a large expansion factor (funnel) because of flux conservation. The flux below the corona (indexed '1') is the same as in the corona (indexed '2') so that $A'_1 n_1 u_1 = A'_2 n_2 u_2$. In a funnel, the cross section A'_1 is smaller than in a coronal hole. And flux conservation is achieved by an increase in

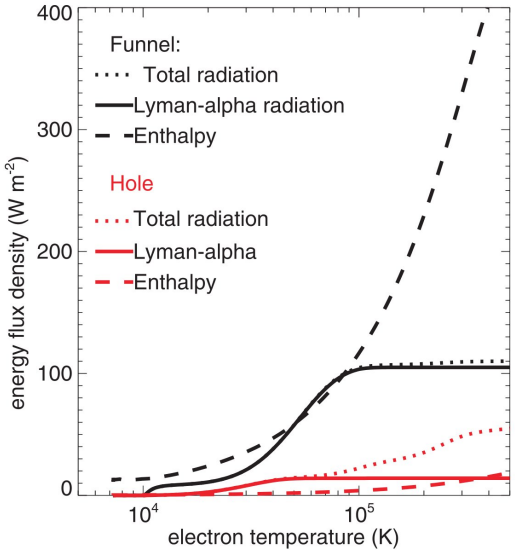

Figure 3.2: **Ly-α**: Radiation loss in the unit of energy flux density, as a function of temperature for a hole geometry (red lines) and a funnel geometry (black lines). Enthalpy flux is higher for the funnel because the outflow velocity is higher. Increased outflow in the funnel carry the Hydrogen atoms further out of ionisation equilibrium to hotter regions where Ly-α loss rate is higher due to much more efficient electron excitation there. From Esser et al. [2005]

the velocity u_1. And because the outflow velocity is much higher the hydrogen is far from ionisation equilibrium. Therefore the Ly-α loss takes place at a higher temperature. As can be seen in the same figure, the enthalpy flux is higher for the funnel than for the coronal hole; in the funnel geometry the downward heat flow from the corona is used primarily to heat the plasma flowing upwards, as opposed to the hole geometry where most of the heat is converted into radiation.

3.2 Byhring et al. [2008]

In Byhring et al. [2008] three geometries have been chosen; two funnel geometries and one coronal hole geometry. One funnel has a very small σ_{g1} (F1), while the other funnel has parameters similar to the funnel in figure 3.1. Observations have revealed that the C and O ions have very low or no

blue shift, and that Ne VIII has blue shifts in the interval $7 - 20$ km s^{-1}. Applying the coronal hole geometry in the model provides too low blueshift for Ne VIII (only 3.5 km s^{-1}). The F2 geometry, on the other hand, provides C and O ions with too large blue shifts. The F1 geometry proves to be the most suitable choice; the blue shifts for all the lines are within the observational values, except for the O V line which is slightly overestimated by the model. The best fit is found for a funnel with an expansion factor of $f_{m2} \sim 4$. The location of the expansion is also found to be important: A sudden expansion should occur *above* the source region of NeVIII. And lower in the transition region, at the forming temperature of C and O, the expansion should be moderate or low.

The lines, the corresponding transitions and the calculated flow velocity from Doppler shifts are reproduced from Byhring et al. [2008] in table 3.1. The Doppler shifts have been calculated by the standard Doppler shift equation $u_d = c(\lambda_0 - \lambda_{max})/\lambda_0$ [10^3 ms^{-1}], where c is the light speed, λ_0 is the natural wavelength of the ion and λ_{max} is the Doppler-shifted wavelength.

Table 3.1: The list of ions, and their wavelength, electronic transitions, formation temperature and the flow velocity. The flow velocity is calculated from observations of Doppler shifts. The velocity values are in [10^3 ms^{-1}]. Although not used in the model by Byhring et al. [2008], the Si II-line has been added for later reference. From Byhring et al. [2008], Tu et al. [2005] and Mazzotta et al. [1998]

Ion	λ_0 [nm]	Transition	$T^{form.}$ [K]	u_d [10^3 ms^{-1}]
Si II	153.3	$3s^2 3p,^2P^O_{3/2} - 3s^2 4s,^2S_{1/2}$	2.0×10^4	-2.0 ± 1.3
C IV	154.8189	$1s^2 2s,^2S_{1/2} - 1s^2 2p,^2P^O_{3/2}$	1.0×10^5	$+0.3 \pm 3.3$
O IV	79.0112	$2s^2 2p,^2P^O_{3/2} - 2s2p^2,^2D_{3/2}$	1.58×10^5	0-3
O IV	79.0199	$2s^2 2p,^2P^O_{3/2} - 2s2p^2,^2D_{5/2}$		
O V	62.9732	$1s^2 2s^2,^1S - 1s^2 2p,^1P^O_1$	2.51×10^5	0-3
O VI	103.7613	$1s^2 2s,^2S_{1/2} - 1s^2 2p,^2P^O_{1/2}$	3.16×10^5	0-10
Ne VIII	77.0409	$1s^2 2s,^2S_{1/2} - 1s^2 2p,^2P^O_{3/2}$	6.3×10^5	$+9.6 \pm 2.0$

3.3 Janse et al. [2007]

Janse et al. [2007] make use of the same computer code as the previous two examples, except that they include helium in their calculations. The inclusion of helium leads to an interesting result. They find that for a large range of heating parameters, the funnel has two co-existing solutions, a slow and a fast solar wind solution that result from the same heating parameters, and depending on the initial state from which the model was started. Although the fast and the slow solar wind can co-exist, it is difficult to change from the fast to the slow solar wind (or vice versa), without a significant change in the heating parameters. And the existence of helium is a requirement for having two co-existing solutions. The scale height of neutral helium in the chromosphere is increased by frictional forces from neutral hydrogen due to the high flow speed in the throat of the funnel. The scale height of the relative heavy helium becomes comparable to that of hydrogen. So the funnel geometry that is chosen in this model is very important for the abundance of helium.

Chapter 4

Examples of Time Dependent Models

In this chapter, two examples of time dependent models will be presented. In time dependent models, the magnetic geometry is no longer considered to be a fixed entity, as in the models of last chapter, but can vary over time.

From a time series of observation with the Michaelson Doppler Imager instrument it has been revealed that small scale regions with opposite polarities not only exist in the photosphere, but move along the internetwork lanes, in the supergranular cells, towards the network lanes by supergranular convection. In the following article by Fisk [2003], these observations are the argument for the model that are presented.

4.1 Fisk [2003]

Fisk [2003] (but also Fisk et al. [1999] and Fisk [2005]) has elaborated on the origin of reconnection in the lower transition region, which may give rise to waves. Fisk [2003] investigates whether the process of displacement of open field lines (of the funnel) can provide the energy and mass needed to form the solar wind. The displacement is due to a coalescence process, in which many small loops are united into larger loops. At some point, these large loops reconnect with open field lines, and the open field lines are displaced to another network lane, or another part of the network lane (figure 4.1). In the A) panel, we see a small loop in development whose foot points move towards the network lane. On both sides of the supergranule, two funnels

expand up from the network lane. The polarity of the left leg of the small loop is opposite of the polarity of the left funnel. B) Given the right conditions, the foot points of the small loop may migrate out toward the network lanes by supergranular convection, and towards a funnel area. If the magnetic field is similar in strength with the funnel magnetic field, the two magnetic structures cancel each other at some point along the left leg of the loop. C) Reconnection occurs, and the field line of the loop opens together with the funnels. At the right side of the loop, the funnel field lines are strengthened because the loop had the same polarity as the funnel. At the left side, the funnel has been weakened by the same amount. Effectively, a certain amount of flux (equal to the loop flux) from the left funnel has been moved to the right funnel, at the expense of the loop. This displacement of open magnetic field lines from one place to another along the surface is occurring all the way up through the corona because the field lines are considered to be stiff.

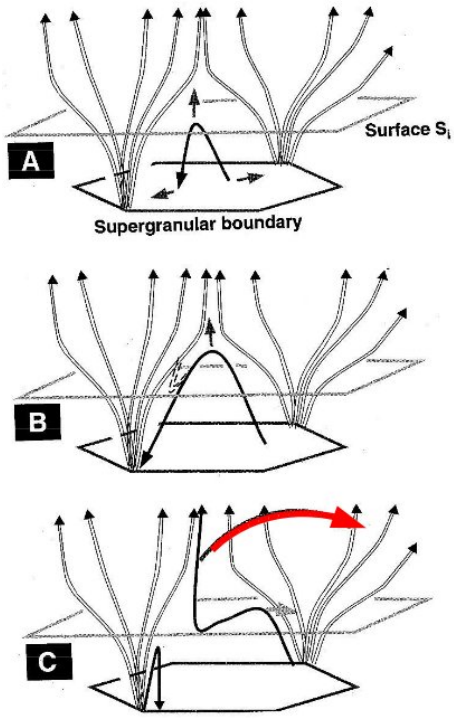

Figure 4.1: **Emerging loops**: A) A new loop emerges, B) Convectional flow carries the loop towards the network lane, where the open field lines are footed, C) reconnection occur, allowing mass to flow into the funnel, and a open field line is displaced (red arrow) to the other side of the network. Illustration from Fisk et al. [1999]

This reconnection process limits the size of loops, and it deposits energy into the corona as well as mass from the loops. It is suggested that the displacement of open field lines in the lower transition region also leads to displacement in the corona. If magnetic flux increases in the 'neck' of one funnel, for example that one to the right in B) in figure 4.1, magnetic flux also increases in the field lines in the corona that are connected to this 'neck' because magnetic flux is conserved along the flux tube ($\mathbf{B}A' = \text{const.}$ where $\mathbf{B}$ is magnetic field strength, A' is cross section of flux tube). If magnetic flux increases in the corona, the energy density and magnetic pressure increase; the volume with a given flux expands, and executes work on the surrounding plasma. Waves may be generated from this

process. The damping of these waves thereby dissipates energy to protons and heavy ions.

In the following, a more detailed presentation will be given on how energy and mass is added by reconnection, in this model by Fisk [2003], and how it influences the speed of the solar wind. An estimate of energy- and mass rate will be given.

Energy: The displacement of open magnetic flux by reconnection of closed field lines with open field lines increases the magnetic flux in the region to which the open field line has been displaced. If one imagines that a surface element $d\mathbf{s}$ contains a foot point of an open field line $\mathbf{B}_{open}$ (e.g. the right funnel in figure 4.1) and the foot point of a closed loop with the same polarity (right foot of the loop in the same figure), reconnection with another open field line outside the surface element (the other field lines being field lines in the left funnel in figure 4.1) doubles the field strength through the surface element to $2\mathbf{B}_{open}$.

In this process, the new field line first oscillates around an equilibrium position. The time it takes for equilibrium to occur after a field line has been displaced is considered to be much shorter than the average period between the displacements of field lines. If we denoted the *displacement period* δt (typically $\sim 10 - 40$ hours), the displacement frequency is $1/\delta t$.

The added magnetic field energy to the corona, $(1/2\mu_0)(B_{open}S_i)\int \mathbf{B}_{open} \cdot d\mathbf{h}$ (in SI-units), is doing work by expanding the surrounding volume, and the energy is converted into other energy forms which heat the corona. In this equation, S_i is the surface element where the field lines pass through as pictured in figure 4.1, $\mathbf{h}$ is the radial vector and μ_0 is the permeability of free space. The above equation is obtained by integrating the energy density of the magnetic field, $(1/2\mu_0)B^2$, along $\mathbf{h}$ and multiplying with a surface element S_i.

The energy rate due to displacement of field lines can then be expressed as,

$$\frac{dE}{dT} = \frac{1}{2\mu_0}\frac{1}{\delta t}(B_{open}S_i)\int \mathbf{B}_{open} \cdot d\mathbf{h} \tag{4.1}$$

where δt is the displacement period as introduced earlier.

Mass: The loops are modelled to be cylinders with cross section S_{loop} and to have a shape like a semi-circle, with radius h_{loop} (height of loops). The base of the loop is defined as the height in which reconnection occurs (the 'floor' in the semi-circle). And z is the height *above* the base. The mass density in the loop is modelled to decrease with height exponentially from the base

(the base is at the level of the surface element S_i in figure 4.1).

$$\rho_{loop} = \rho_{loop,i} \exp[-z(GM_0 m_p / 2r_0^2 kT)] \tag{4.2}$$

where $\rho_{loop,i}$, G, M_0, m_p, r_0, k and T is the mass density at the base, gravitational constant, mass of the sun, mass of the proton, radius of the sun, Boltzmann's constant and the temperature of the loop, respectively. Equation (4.2) has been derived from the assumption of hydrostatic equilibrium, i.e. that the force of gravity equals the pressure force from below at any height in the loop.

The total mass M of the loop is obtained by integrating equation 4.2 from the base to h_{loop} and multiplying with S_{loop},

$$M_{loop} = \rho_{loop,i} S_{loop} \left(\frac{2r_0 kT}{GM_S m_p} \right) [1 - \exp(-1.75 h_{loop} GM_S m_p / 2r_0^2 kT)]$$

S_{loop}, the cross sectional area of the loop that undergo reconnection, can be defined as $S_{loop} = S_i(B_{open,i}/B_{loop,i})$, where B_{loop} is the magnetic field strength in loops. The mass rate dM/dt can now be achieved by multiplying M with $1/\delta t$, and substituting for S_{loop},

$$\frac{dM}{dt} = \left(\frac{\rho_{loop,i}}{B_{loop,i}} \right) \left(\frac{B_{open,i} S_i}{\delta t} \right) \left(\frac{2r_0 kT}{GM_S m_p} \right) [1 - \exp(-1.75 h_{loop} GM_S m_p / 2r_0^2 kT)] \tag{4.3}$$

Fisk [2003] argues that dM/dt must be constant, because the mass flux ρu at 1 AU is approximately constant. The mass rate in equation(4.3) has the unit of [kg s^{-1}]. This can also be written as [(kg m^{-3})(ms^{-1})(m^2)] which is mass flux multiplied with an area. The mass flux $\rho_i u_i$ can the be obtained by multiplying (4.3) with $1/S_i$,

$$\rho_i u_i = \left(\frac{\rho_{loop,i}}{B_{loop,i}} \right) \left(\frac{B_{open,i}}{\delta t} \right) \left(\frac{2r_0 kT}{GM_S m_p} \right) [1 - \exp(-1.75 h_{loop} GM_S m_p / 2r_0^2 kT)] \tag{4.4}$$

The mass flux of the solar wind is, with equation (4.4), related to the temperature of the loop T, the height of the loop, the relative field strength and the mass density of the loop.

The solar wind speed. In the model by Fisk [2003] the solar wind is assumed to be a single MHD fluid with mass density ρ and velocity $\mathbf{u}$. Below

energy flux balance equations will be presented. Two cylindrical surfaces perpendicular to the magnetic field through which energy flux flows is considered: The outer surface, S_o, situated where the solar wind has achieved its full speed ($\sim 10\ R_S$), and an inner surface, S_i, through which mass flows, and waves propagate (figure 4.2). Both of these surfaces are small enough for the plasma parameter to be uniform in the time averaged sense. S_i must however be large enough to cover the region where displacement of field lines occurs.

The energy flux can be expressed as,

$$\left\langle \rho \mathbf{u} \frac{u^2}{2} \right\rangle \cdot S_0 = \langle \mathbf{P} \rangle \cdot S_i - \frac{GM_0}{r_0} \langle \rho \mathbf{u} \rangle \cdot S_i \tag{4.5}$$

In equation (4.5), $\langle \mathbf{P} \rangle$ is the time averaged Poynting vector which describes the energy flux per. unit area of a wave, [W/m^2]. The expression on the left side is the time averaged kinetic energy flux ('energy per second') of the solar wind, [(kg m^{-3})(ms^{-1})(m^{2}s^{-2})(m^2) which equals kg m^{2}s^{-2}s^{-1}='energi per second']. The first term on the right hand side is the Poynting vector, ie. the wave-energy flux, [W] ('energy per second'), of the upward propagating Alfvén waves, that are assumed to be the mechanism that dissipate energy in the corona. The second term is the energy flux that accounts for the loss of energy with distance due to gravitation, [kg m^{2}s^{-2}s^{-1}] ('energy per second').

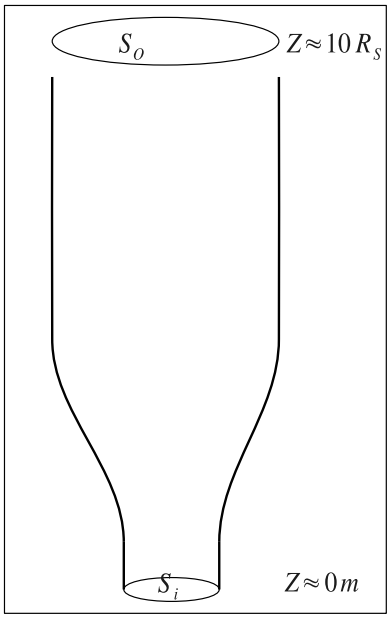

Figure 4.2: **Mass and energy flow**: Illustration of the surfaces through which energy and mass flow

Equation (4.5) states that the energy that ultimately leaves the corona in the solar wind, per second, is the same as the energy that is supplied to the corona, per second. It is important to have in mind that the reason why heat conduction is not included in (4.5) is because the described process takes place far above the surface S_i. In other words, it is the net energy flux that is considered. Heat conduction does not reach down to the

surface S_i. However, in (4.5), the kinetic energy of the mass flow in the funnel has been neglected. Although small, it is a contribution to the energy budget. Secondly, it is assumed that the Poynting vector is strictly parallel to the magnetic field lines. As a third point, the model assumed that all the net energy input is specified in the Poynting vector only, an assumption that may perhaps be too simple. And the model also assumes that all energy from the corona consists only of flow energy of the solar wind.

Another condition that is applied is the conservation of mass flux,

$$\langle \rho \mathbf{u} \rangle \cdot S_o = \langle \rho \mathbf{u} \rangle \cdot S_i \tag{4.6}$$

If the indexes o and i are applied to the $\langle \rho \mathbf{u} \rangle$ terms in equation (4.6) and (4.5), substitute S_o and S_i in (4.5) with the respective relations in equation (4.6), comparing and cancelling re-occurring factors, the following expression will result,

$$\frac{u_o^2}{2} = \frac{P_i}{\rho_i u_i} - \frac{GM_0}{r_0} \tag{4.7}$$

As can be seen from equation (4.7), the square of the solar wind velocity depends inversely upon the mass flux at the base, $\rho_i u_i$ and the Poynting vector. The Poynting vector can be related to the energy rate due to displacement of magnetic field. If equations (4.1) and (4.4) is inserted into (4.7),

$$\frac{u_o^2}{2} = \left(\frac{B_{loop,i}}{\rho_{loop,i}} \right) \left(\frac{\int \mathbf{B}_{open} \cdot d\mathbf{h}}{2\mu_0 r_0} \right) \left(\frac{GM_0 m_p}{2 r_0 kT} \right) \beta(h_{loop}, T) - \frac{GM_O}{r_0} \tag{4.8}$$

where $\beta(h_{loop}, T) = \{1 - \exp\left[-(1.75 h_{loop} GM_0 m_p)/(2r_0^2 kT)\right]\}^{-1}$.

From equation (4.8) it can be read that $u^2 \propto 1/T$. The factor $B_{loop,i}/\rho_{loop,i}$ is considered to be constant, because large loops with strong fields also have a higher density at the base. The integral in the second factor is also constant along the field line. From observations it is known that the height of loop h_{loop} is proportional to the temperature in the loops. The function $\beta(h_{loop}, T)$ is then thought to be weakly a function of T only. So the final speed of the solar wind depends primarily on the temperature in loops, and u^2 varies as $1/T$.

4.2 He et al. [2008]

He et al. [2008] develop a model based on observations (from e.g. Tu et al. [2005]) that mass and energy seems to be supplied at a height of 5×10^6 m.

He et al. [2008] assume that loops reconnect with the funnel at this height. In this process, mass from the loop is deposited into the corona, and the energy input is determined from the energy flux associated with the reconnection.

One of the arguments by He et al. [2008] is that their type of geometry can explain inflow and outflow, as manifested by the observed red and blue shifts. These Doppler shifts for Si II, C IV and Ne VIII from Tu et al. [2005] are included in table 3.1. The height of the maximum emission from these three lines was found by Tu et al. [2005], by correlation between emission maps and Doppler maps, to be 4×10^6 m, 5×10^6 m and 24×10^6 m for Si II, C IV and Ne VIII, respectively. The downward flow velocity is calculated mainly from red shifts of Si II. The upward flow is calculated similarly from observation of blue shifts of Ne VIII.

The observations of no significant Doppler shift at 5×10^6 m can be interpreted, according to He et al. [2008], as a scenario in which mass is supplied at this height by reconnection with the neighbouring network loops. A cartoon of this process is re-produced in figure 4.3. This figure illustrates how the lower corona/transition region in the funnel is supplied with mass by reconnection with loops. In this figure, the reconnection will occur at the point where the field lines of the loop and the funnel are closest (at $z \approx 5 \times 10^6$ m). The region below this reconnection point is called region 1 by He et al. [2008]. The region above this point is region 2. The reconnection itself has been explained earlier, in figure 4.1. This figure is presented to emphasise where the mass and energy is deposited, the process that transport loops towards the network lanes and the direction of the flow. Details geometry, the loops, mass input rate, etc, will be given below

The degree of expansion of the geometry is very important for the outflow. An increase in expansion results in increased outflow (due to flux conservation, $A'nu$ = const.). At the same time, the mass flux must satisfy other conditions, such as the boundary conditions at 1 AU. The model by He et al. [2008] suggests a geometry that is thought to fit best to the observation of upflow.

The vertical field strength as a function of height ($B_z(z)$) consists of two components,

$$B_z(z) = B_{funnel}(z) + B_{global}(z) \tag{4.9}$$

The funnel component dominates $B_z(z)$ in the lower region from the photosphere to $\approx 20 \times 10^6$ m, while the global component dominates in the upper

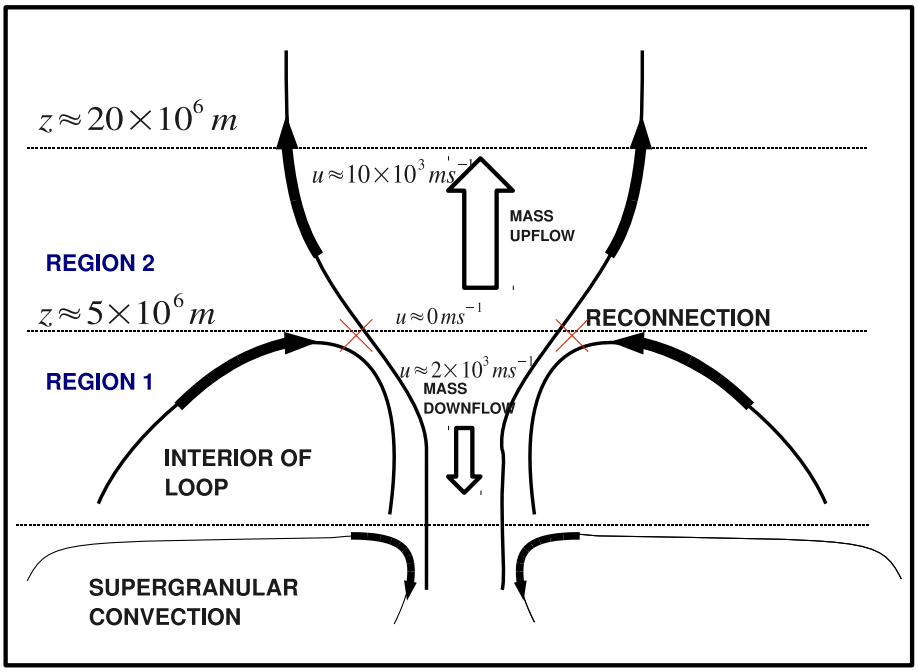

Figure 4.3: **Mass outflow**: Mass outflow as described by He et al. [2008]. The black lines above the photosphere are magnetic field lines, while the lines below the photosphere are the convectional flow direction. The black arrows indicate direction of field lines/flow. Big arrows are flow direction of plasma in the funnel. Supergranular convection transports loops towards the network lanes. As the field lines of the loop and the funnel have opposite polarity at the reconnection point, and given that the magnetic flux is the same, the loops reconnect with the funnel at height $z = 5 \times 10^6$ m. Mass from the loops is released into the funnel. A small part of the mass flux is directed downward, while the largest part is directed upward. The flow velocities in this figure is from He et al. [2008], but based on results from Tu et al. [2005]

region from $\approx 20 \times 10^6$ m. The two components are explicitly given as,

$$B_{funnel}(z) = b_0 \exp(b_1 z) \tag{4.10}$$

$$B_{global}(r) = M\left[\frac{2}{r^3} + \frac{3Q}{r^5} + \frac{K}{a_1(r+a_1)^2}\right] \tag{4.11}$$

In equation (4.10) the parameters $b_0 = 56.5$ G and $b_1 = -0.28 \times 10^6$ m^{-1} are parameters that are used to fit the field strength values to observed ones at the boundaries. In equation (4.11) r is normalized distance ($r = (z/R_S)+1$). The first term describes the contribution from the dipolar magnetic field of the sun. The second term describes quadrupolar distribution, and the third – current-sheet distribution. The parameters are defined as $M = 1.789$ G, $Q = 0.26$, $K = 1.0$ and $a_1 = 1.538$, and they are used to adjust the different distributions to observed values.

The governing fluid equations in the model are as follows,

$$\frac{\partial}{\partial z}(\rho u A) = 0 \tag{4.12}$$

$$\rho u \frac{\partial}{\partial z} u = -\frac{\partial}{\partial z}(P + P_A) - \rho g \tag{4.13}$$

$$\frac{u \cdot 2nk}{\gamma - 1}\frac{\partial}{\partial z}T + \frac{2nkT}{A}\frac{\partial}{\partial z}(Au) = -L_r + H - \frac{1}{A}\frac{\partial q}{\partial z} \tag{4.14}$$

These equations (4.12-4.14) describe the conservation of mass, momentum and energy. These set of equations may have different parameters for region 1 and region 2. The parameters in the equations, A, q, P, L, H and P_A are the cross sectional area of the flux tube, thermal conduction flux, thermal pressure, the radiation loss, the heating function and Alfvénic wave pressure, respectively. The radiation loss [ergs cm^{-3} s^{-1}] is defined in the same way as in Rosner et al. [1978].

The heating function $H(z)$ is proportional to the upper threshold frequency of the waves. Examples of heating functions are shown in figure 4.4. The upper threshold frequency of the waves depends on the gas pressure. Since the gas pressure approximately decreases exponentially with height, so does the heating function as is seen in the near-linear shape of the curve in the logarithmic scale of figure 4.4.

The Alfvénic wave pressure is defined as,

$$P_A = \frac{\langle \delta B^2 \rangle}{8\pi}$$

By the method of Hackenberg et al. [2000], the fluid equations (4.12-4.14)

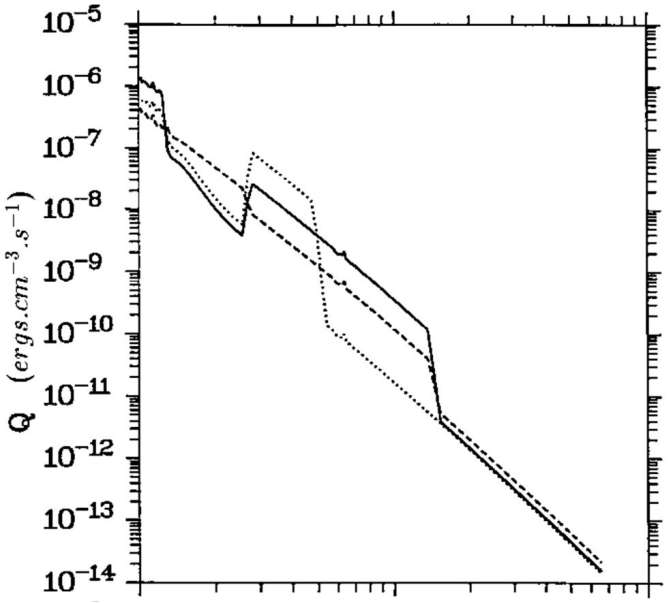

Figure 4.4: **Heating functions**: Example of heating function $H(z)$ calculated from different models of Tu and Marsch [1997]. The non-smooth shape of these curves are model artefacts from the piecewise $f(z)^{-1}$ dependence of the heating function. The 'Q' on the y-scale is the same quantity as $H(z)$. The x-scale starts at $1R_S$ and ends at $100R_S$. From Tu and Marsch [1997]

can be transformed into a closed set of ordinary differential equations,

$$\frac{d\rho}{dz} = \frac{\rho}{dz}\frac{\dot{M}^2 A' + A^2\rho^2(2k/m_p)(q/\kappa) - A^3\rho^2\tilde{g}}{A^2\rho P_{eff} - \dot{M}^2} \tag{4.15}$$

$$\frac{dT}{dz} = -\frac{q}{\kappa A} \tag{4.16}$$

$$\frac{dq}{dz} = A(H - L_r) + \frac{\dot{M}k}{m_p}\left(\frac{2T\rho'}{\rho} - \frac{2T'}{\gamma - 1}\right) \tag{4.17}$$

In equations (4.15-4.17), $\dot{M}$, A', κ, $\tilde{g}$, P_{eff}, ρ' and T' are the mass flux, expansion gradient dA/dz, the thermal conduction coefficient ($\propto T^{5/2}$), the effective gravitational acceleration, the total effective pressure (which depends on the wave pressure P_A), mass density gradient $d\rho/dz$ and temperature gradient dT/dz, respectively.

The mass density and velocity at the boundary of region 2 is set at $\rho^0 =$

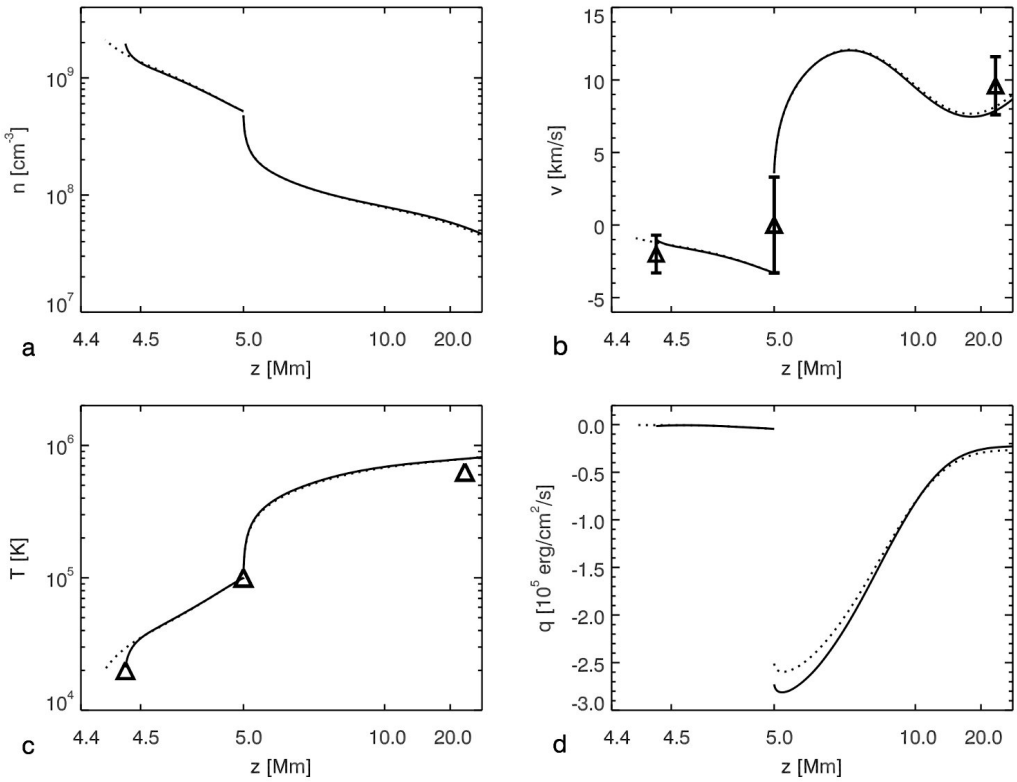

Figure 4.5: **Model results He et al. [2008], lower region**: Variation of the plasma parameters n, u and T with height in region 1 and beginning of region 2. The solid lines are for the boundary wave pressure $P^0_{A,1}$, and the dotted lines are for $P^0_{A,2}$ (defined in text). a) The number density n. b) The outflow velocity. The three triangles are the Doppler velocity for the observed shifts from Si II (red shifts), C IV (near zero shifts) and Ne III (blue shifts), respectively, and their corresponding error bars. c) Temperature. The three triangles are the formation temperature for the three ions. d) Thermal conduction flux. From He et al. [2008]

8.65×10^{-13} kg m^{-3}, and $u^0 = 3.3 \times 10^3$ ms^{-1} so that it both satisfies the mass rate input from the loops, and the boundary conditions at 1 AU. The temperature at the boundary of region 2 is determined at $T^0 = 1 \times 10^5$ K. Since we know that C IV is formed at this height, the temperature at this height is found from the formation temperature for this line in table 3.1. Two set of results are calculated, for two examples of boundary conditions for the wave pressure P_A, $P^0_{A,1} = 0.52 \times 10^{-2}$ [10^4 dyn m^{-3}] and $P^0_{A,2} = 0.45 \times 10^{-2}$

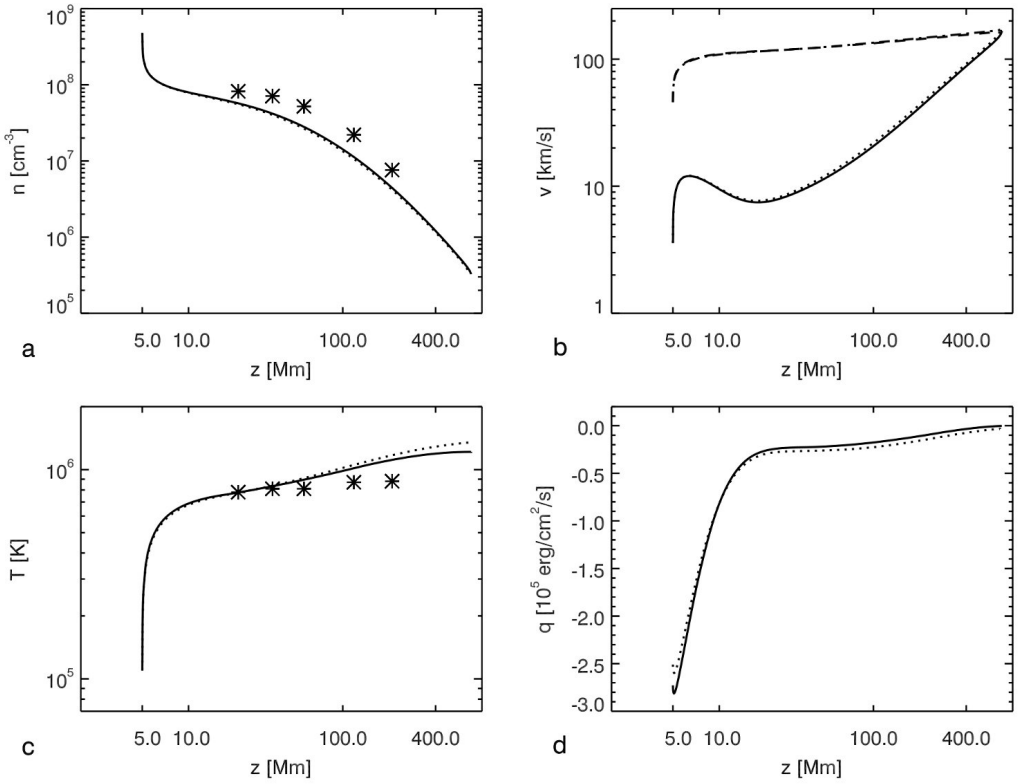

Figure 4.6: **Model results He et al. [2008], upper region**: Same as in figure 4.5, but for the upper height region, and showing region 2 only. The asterisks in a) are densities deduced from observations (Wilhelm et al. [1998]). The dashed line in b) is the sound speed. And the asterisks in c) are also temperatures deduced from observations (Wilhelm et al. [1998]). From He et al. [2008]

[10^4 dyn m^{-3}].

Solving the equations (4.15-4.17) with these boundary conditions yields the temperature, density and flow velocity, as shown in figures 4.5 and 4.6.

In these figures we see the result of the model by He et al. [2008]. Two set of results for each plasma parameters, for the boundary values of the wave pressure ($P^0_{A,1}$ and $P^0_{A,2}$), are plotted. We see that the plasma parameters change considerable at the boundary between region 1 and 2, at 5×10^6 m. For example, the outflow velocity increases rapidly between 5 and 6×10^6 m and reach a maximum of 13×10^3 ms^{-1} already at 8×10^6 m. In the figures,

observed values of the parameters are also plotted for comparison.

To test the model by He et al. [2008] we will use the parameters shown in the figures 4.5 and 4.6 to calculate the Doppler-shift of the spectral lines given in table 3.1.

4.3 Evaluation of the Velocity Constraints

In order to evaluate the velocity constraints we should calculate the ionisation balance of Si II, C IV and Ne VIII ions first. We assume that the ion flow velocity will be the same as the proton flow velocity. This is a good assumption in a *funnel geometry* below $r \approx 1.08 R_S$ (e.g. Byhring et al. [2008] show that the proton outflow velocity is coupled to that of the O VI ion up to $r \approx 1.08 R_S$ in figure 2 in their work).

4.3.1 Ionisation Balance and Spectral Line Source Region

The equation for density of the ions is (Esser and Edgar [2001]),

$$\frac{1}{A}\frac{\partial}{\partial r}(n_i u_i A) = n_e[n_{i-1}C_{i-1} - n_i(C_i + R_i) + n_{i+1}R_{i+1}] \tag{4.18}$$

In equation (4.18) n_i is the density of the ion in question, and n_{i-1} is the density of the ion with one degree lower ionisation than the ion, and n_{i+1} is the density of the ion with one degree higher ionisation than the ion. C_i [cm^3 s^{-1}] is the ionisation rate of the ion (rate of transitions $i \rightarrow i+1$ by ionisation) and R_i [cm^3 s^{-1}] is the recombination rate of the ion (rate of transitions $i \rightarrow i-1$ by recombination). We have used the C_i and R_i rates from Mazzotta et al. [1998]. The geometry A is the same as $B(z)$ which has already been defined in equation (4.9).

Around the formation temperature Si II and C IV in region 1 we already know that downflow is negligible. The observed and modelled Doppler shift velocities (Tu et al. [2005] and He et al. [2008]) are almost zero in this temperature region. We may then assume $\partial(n_i u_p A)/\partial r \rightarrow 0$. The left side of equation (4.18) can be neglected. If we denote n_0 the density of a neutral element (X I for the element X), and n_1 the density of the ion X II and so

on, we can write out equation (4.18) for the neutral and first ionisation stage,

$$-n_0 C_0 + n_1 R_1 = 0 \tag{4.19}$$

$$n_0 C_0 - n_1 C_1 - n_1 R_1 + n_2 R_2 = 0 \tag{4.20}$$

For equations (4.19-4.20) we get the fractions,

$$\frac{n_1}{n_0} = \frac{C_0}{R_1} \tag{4.21}$$

$$\frac{n_2}{n_1} = \frac{C_1}{R_2} \tag{4.22}$$

where equation (4.22) has been obtained by substituting $n_1 R_1$ in equation (4.20) by $n_0 C_0$ from (4.19). A fraction n_2/n_0 can easily be obtained from the above equations. By continuing to write the equations for higher ionisation, we get the general equations,

$$\frac{n_m}{n_{m-1}} = \frac{C_{m-1}}{R_m} \tag{4.23}$$

$$\frac{n_m}{n_0} = \prod_{k=1}^{m} \frac{C_{k-1}}{R_k} \tag{4.24}$$

Here m is the degree of ionisation ($m = 0, 1, 2, 3, 4...$) where $m = 0$ is neutral. For example $n_1 = n_{\mathrm{X\ II}}$ of the element X. Other combinations of fractions can be found be combining equations (4.23) and 4.24.

The energy flux per unit wavelength λ from an emission line is (Byhring et al. [2008]),

$$I(\lambda) = a \int_{R_{low}}^{R_{high}} P(r, \lambda) dr \tag{4.25}$$

where R_{low} and R_{high} is the lower and upper height of the model (in this section, "r" denotes radial distance above the limb). The function $P(r, \lambda)$ (the spectral line source region) is defined as,

$$P(T_e, \lambda) = n_i n_e C_i \frac{hc}{\lambda_0} \frac{1}{\sqrt{\pi} \Delta\lambda_D} \exp\left\{ - \left[\frac{\lambda - \lambda_0 + (\lambda_0 u_i / c)}{\Delta\lambda_D} \right]^2 \right\} \tag{4.26}$$

where r has been converted to T_e. This equation describes the power per unit volume and wavelength [Wm^{-4}] of a spectral line as a function of temperature. In the above equation, λ is the wavelength of the emission line,

λ_0 the wavelength of the line in the rest frame (given in table 3.1) and $\Delta\lambda = (\lambda_0/c)\sqrt{(2kT_e/m_i)}$.

While an ion fraction n_i/n of an ion merely is a measure of the fraction of the amount of ion particles to the total number of element particles, equation (4.26) is a more complex quantity that give us information on where the line has highest intensity, and it depends on variables such as the electron density (which excites the ions) and λ.

For each temperature/height we will find the value of $P(T_e, \lambda)$ at which $P(T_e, \lambda)$ has a maximum as a function of λ. These P-values are then divided of the maximum of all of them, so that,

$$\frac{P(T_e, \lambda_{max})}{\max(P(T_e, \lambda))} \tag{4.27}$$

defines the emission line source region. λ_{max} is the value of λ at which $P(T_e, \lambda)$ is maximum.

4.3.2 Results for Si II

We are now in position to find the ionisation balance for the II ion. With ionisation balance we mean the fraction of the density of Si II to the total density of Si (all ions of Si), $n_{\mathrm{Si\ II}}/n_{\mathrm{Si}}$. The total density of the element Si, n_{Si}, is,

$$n_{\mathrm{Si}} = n_{\mathrm{Si\ I}} + n_{\mathrm{Si\ II}} + n_{\mathrm{Si\ III}} + n_{\mathrm{Si\ IV}} \tag{4.28}$$

where we have assumed that ions higher than Si IV can be neglected in this temperature region $10^4 < T < 10^5$ K. To get the ion fraction of Si II we can multiply equation (4.28) with $(1/n_{\mathrm{Si\ II}})$ on both sides. The following expression (4.29) then yields the ion fraction,

$$\begin{aligned}
\frac{n_{\mathrm{Si\ II}}}{n_{\mathrm{Si}}} &= \left[\left(\frac{n_{\mathrm{Si\ II}}}{n_{\mathrm{Si\ I}}}\right)^{-1} + 1 + \frac{n_{\mathrm{Si\ III}}}{n_{\mathrm{Si\ II}}} + \frac{n_{\mathrm{Si\ IV}}}{n_{\mathrm{Si\ II}}}\right]^{-1} \\
\frac{n_{\mathrm{Si\ II}}}{n_{\mathrm{Si}}} &= \left[\left(\frac{C_{\mathrm{Si\ I}}}{R_{\mathrm{Si\ II}}}\right)^{-1} + 1 + \left(\frac{C_{\mathrm{Si\ II}}}{R_{\mathrm{Si\ III}}}\right) + \left(\frac{C_{\mathrm{Si\ II}} C_{\mathrm{Si\ III}}}{R_{\mathrm{Si\ III}} R_{\mathrm{Si\ IV}}}\right)\right]^{-1}
\end{aligned} \tag{4.29}$$

In equation 4.29 we have used the equations (4.23) and (4.24).

The ionisation fraction, as defined in equation (4.29), is plotted in figure 4.7 upper panel. The blue line in this panel is the ion fraction for Si II

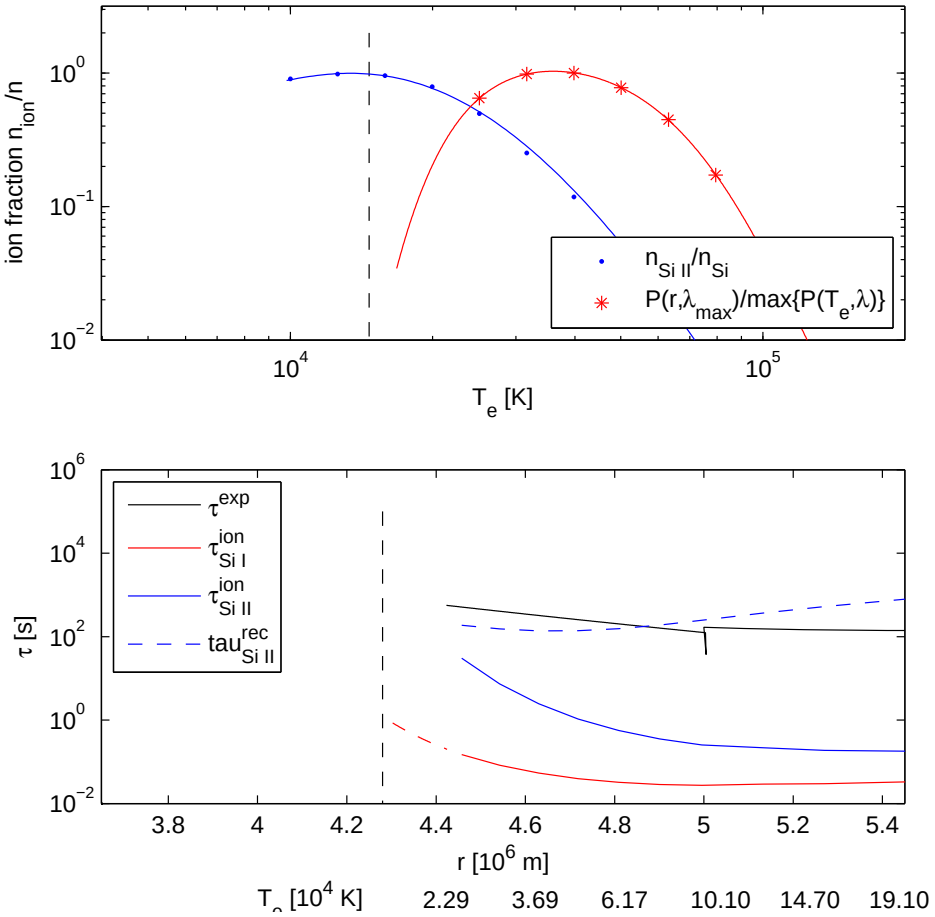

Figure 4.7: **Si** II: Upper panel: Ion fraction (blue) and emission line source region (red) of Si II. Calculation is done by using equation (4.23),(4.24), (4.29) and (4.27). The ion fraction is based on C_i and R_i rates from Mazzotta et al. [1998] which are provided for the temperature $\log_{10}(T) = 4.0, 4.1, 4.2....$ The vertical black dashed line is $T^{form.}_{\text{Si II}}$. Lower panel: τ as a function of r. The vertical black dashed line is $r^{form.}_{\text{Si II}}$.

calculated from equation (4.29). The reason why the fraction only begin from 10^4 K is because the temperature dependent C_i and R_i rates that have been used (Mazzotta et al. [1998]) are not provided for lower temperatures. The vertical dashed line marks the maximum of Si II, which can be seen to

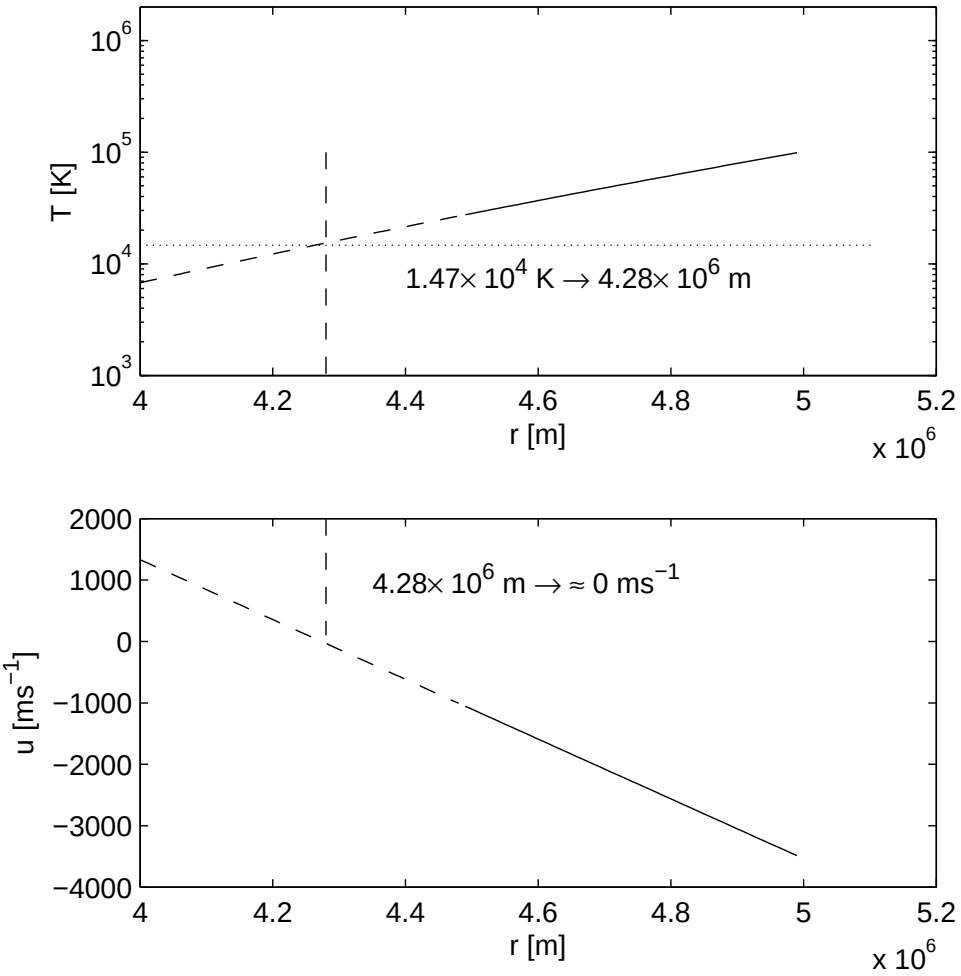

Figure 4.8: **Region 1**: Upper panel: Temperature as a function of height. The solid line is the data from He et al. [2008]. The non-vertical dashed line is the extrapolation from He et al. [2008]. The horizontal dotted line is $T^{form.}_{\text{Si II}}$. The vertical dashed line is $r^{form.}_{\text{Si II}}$. Lower panel: Intersection of $r^{form.}_{\text{Si II}}$ with the extrapolation of the velocity yields zero flow.

occur at,

$$T^{form.}_{\text{Si II}} \approx 1.47 \times 10^4 \text{K}$$

which corresponds to a height of $r_{\text{Si II}}^{form.} \approx 4.28 \times 10^6$ m. The $T_{\text{Si II}}^{form.}$-value differs a bit from the value in Tu et al. [2005] and He et al. [2008], a difference that can arise from the usage of different C_i and R_i data sets. In addition, these formation values are outside the temperature/height range in the model by He et al. [2008] (figure 4.5), in which the lowest temperature and height is 2×10^4 K and $\approx 4.45 \times 10^6$ m. But we may extrapolate the temperature in region 1 in figure 4.5, down the temperature gradient. Doing this, we find the height at which the temperature intersects with $T_{\text{Si II}}^{form.}$. This is shown in figure 4.8 upper panel. By extrapolating u we find that this height corresponds to a velocity of ≈ 0 ms^{-1} (figure 4.8 lower panel). In other words, the equilibrium formation temperature $T_{\text{Si II}}^{form}$ correspond to a height where there is almost no flow. This is also almost in agreement with observations ($-2.0 \pm 1.3 \times 10^3$ ms$^-1$ in table 3.1).

The red line in the upper panel of figure (4.7) is the emission line source region, as defined in equation (4.27), for Si II. The emission peaks at $\approx 3.5 \times 10^4$ K, which is a bit hotter than $T_{\text{Si II}}^{form.}$, but not much. In additional to the normalised value of $P(T_e, \lambda)$, the shape of this function reveals information about the impact of flow on the wavelength from the line. In figure 4.9 we see that for low temperatures (low height), the shift $\Delta\lambda = \lambda_0 - \lambda_{max}$ is small, and for high temperature the shift is larger, which is in accordance with the velocity parameter in panel b in figure 4.5. A negative $\Delta\lambda$ confirms that there is downflow in region 1. We have also compared this shift $\Delta\lambda$ at the temperature $T_{\text{Si II}}^{form.}$ with the shift $\lambda_0 - \lambda_{max} = u\lambda_0/c$ and found that they approximately coincide.

To test whether it can really be justified to assume zero flow ($d(n_i u_p A)/dr = 0$), we can analyse the ionisation-, recombination- and expansion time scales for the Si ion and to compare them. These are given by Esser and Edgar [2001] and they are $\tau^{ion} = 1/(C_i n_e)$, $\tau^{rec} = 1/(R_i n_e)$ and $\tau^{exp} = (n_e/u_i)(dn_e/dr)^{-1}$, respectively. τ^{ion} and τ^{rec} reveal how long time, on average, it takes to further ionise or recombine an ion at a given temperature (or height). The expansion time scale τ^{exp} shows how long time it takes for a plasma element to relocate a scale-height by outflow.

Figure 4.7 lower panel shows these time scales as a function of height. τ^{exp} (solid black line) is the same for all ions because we have assumed $u_i = u_p$. τ^{ion} (coloured solid lines) is plotted for the ions Si I (red) and Si II (blue). $\tau_{\text{Si II}}^{rec}$ (blue dashed line) is also shown. The ionisation times decrease with altitude, as expected, and the ionisation time for Si II is longer than for Si I, at a given height/temperature, which is also expected since higher energy

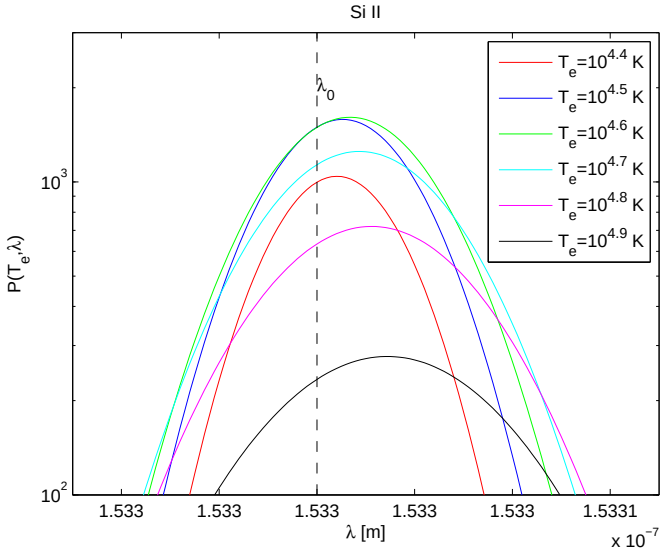

Figure 4.9: **The emission from Si II for a selection of T_e**: The emission $P(T_e, \lambda)$ as a function of λ for some temperatures. The vertical black dashed line is λ_0 for Si II.

(more of fast moving electrons) is required to further ionise the former ion than the latter one. Since the production of Si III ions are so infrequent (the $\tau^{ion}_{\text{Si II}}$ time scale is relatively long in this region), recombination from Si III to Si II ($\tau^{rec}_{\text{Si III}}$) has been considered unnecessary to include. In the figure the formation temperature is converted to height ($r^{form.}_{\text{Si II}}$), indicated with a dashed black line in the lower panel, but a temperature scale is left for comparison. As before, the formation temperature(/height) is below the lowest height found in the model of He et al. [2008], but an extrapolation (red dashed line) has been plotted for $\tau^{ion}_{\text{Si I}}$. τ^{exp} is not extrapolated, but it can be seen that it carries on almost horizontally in negative height direction. The most relevant information that can be obtained from the lower panel in this figure is that, at $r^{form.}$, $\tau^{ion}_{\text{Si I}}$ is $\approx 10^3$ s shorter than τ^{exp}. In other words, The time it takes to produce Si II by ionisation is much faster than the time it takes to relocate the plasma one scale height. The recombination from Si II (loss of Si II) is quite slow compared to ionisation the time scale, but still faster than the expansion time. The assumption of zero flow, on which the ionisation fraction in panel 1 is based, can therefore be said to be justified.

4.3.3 Results for C IV

From table 3.1 in chapter 3 it can be deduced that C IV forms at the border between region 1 and 2 (at $T_e = 1 \times 10^5$ K). The Doppler shift velocity that Byhring et al. [2008] find for C IV (-2.7×10^3 ms^{-1} in model 'F1') very much agrees to the outflow in the end of region 1 of the model by He et al. [2008] (-3.0×10^3 ms^{-1} at $r = 5 \times 10^6$ m or $T = 1 \times 10^5$ K). The method that is used by Byhring et al. [2008] involves integrating along the line-of-sight (along different vertical layers). And the actual Doppler shift velocity at, say at $r = 5 \times 10^6$ m, may not be correctly estimated since different layers of the atmosphere contributes in the calculation. The line-of-sight effect may be strong especially when the ion fraction temperature-width is large, such as in the case of C IV. However, since the output Doppler shift velocity parameters agree so much between the two models, even for C IV, we may assume that the line-of-sight effect is weak or negligible. This opens up the opportunity to compare our results of ion fractions with the results from Byhring et al. [2008].

The flow velocity at $r = 5 \times 10^6$ m is uncertain, because of large error margins in the observations ($0.3 \pm 3.3 \times 10^3$ mss^{-1} in Tu et al. [2005]/table 3.1). And whatever outcome our analysis yields, it will not be able to constrain observations very much, since the formation region is in a region where the model has a discontinuity. But if we assume that the flow is zero, we can apply the equations already developed in this section to calculate the ion fraction. In the same way as in equation (4.28) we write the density for each ionisation stage of Carbon, except that we add more terms, including $n_{\text{C VI}}$ to ensure that no ion density contributions are left out. Such a 6-term equation is multiplied with $(1/n_{\text{C IV}})$. The terms in the equation that results from this is then replaced according to equations (4.23–4.24), in the same way with Si II.

The ion fraction for C IV is shown in figure 4.10 upper panel as a blue line. As can be seen from this figure,

$$T^{form.}_{\text{C IV}} \approx 1.00 \times 10^5 \text{K}$$

In Tu et al. [2005] it was found that C IV forms at $r \approx 5.0 \times 10^6$ m. If we convert $T^{form.}_{\text{C IV}}$ to height according to the model by He et al. [2008], figure 4.5 panel c, we find an exact match: C IV does seem to have maximum abundance at $r \approx 5 \times 10^6$ m. Thus, from this comparison the model by He et al. [2008] has proved to match observations, and our ion fraction calculation, in a good

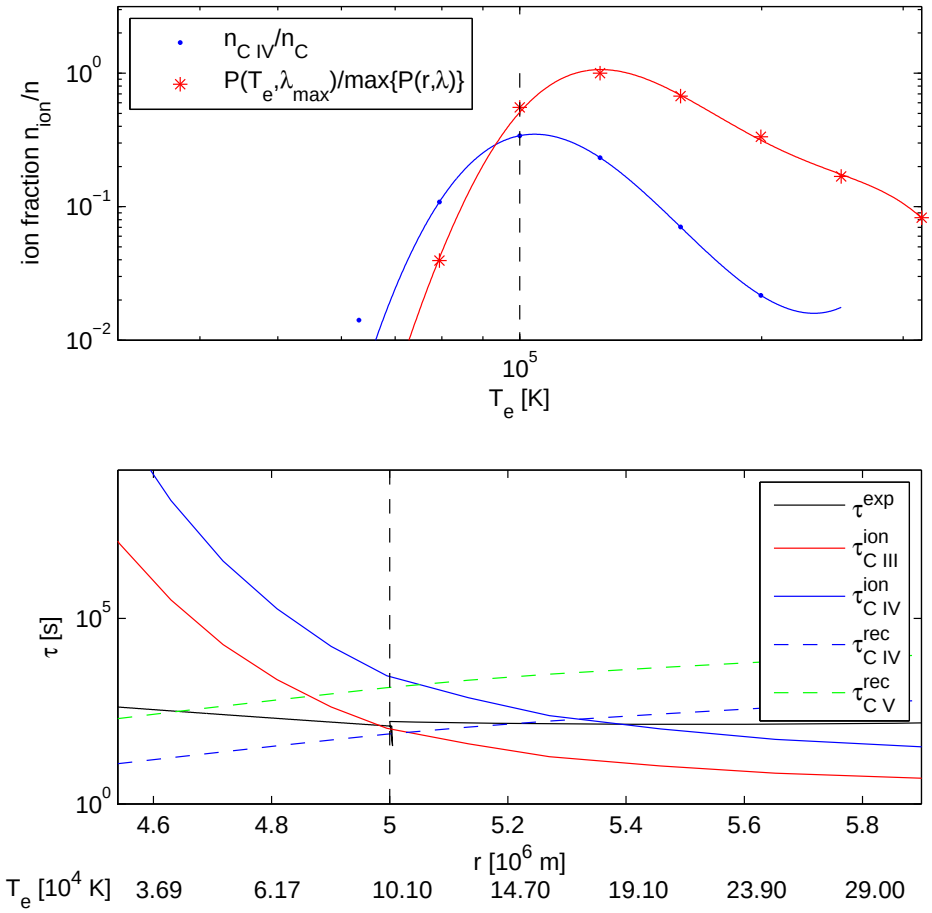

Figure 4.10: **C** IV: Upper panel: Ionisation fraction and line source region of C IV as a function of temperature. The vertical dashed black line is $T^{form.}_{\mathrm{C\ IV}}$. Lower panel: Time scales as a function of height and temperature. Here, the vertical dashed black line is $r^{form.}_{\mathrm{C\ IV}}$.

way.

In addition, Byhring et al. [2008] find a equilibrium formation temperature of C IV of 0.9×10^5 K, very close to our result and He et al. [2008].

The line intensity is also shown in the upper panel of figure (4.10), as a red line. The source region of the intensity can be seen to be at $\approx 1.5 \times 10^5$ K.

If there is outflow or downflow at $r^{form}_{\text{C IV}}$ (there may be up to 3.6×10^3 ms^{-1} outflow, or -3.0×10^3 ms^{-1} downflow according to observations), then a test with time scales calculations should be performed, as was done with Si II. Time scale calculation is shown in figure 4.10 lower panel. Here we see that, at the formation height, ionisation from C III to C IV and recombination from C IV to C III is at the same level as the expansion time. Based on this, it is likely that C IV is in ionisation equilibrium. The ion fraction shown in the upper panel, to which the assumption of zero flow has been applied, is at least a good approximation.

4.3.4 Results for Ne VIII

In the formation height region of Ne VIII there is certainly a considerable outflow. So the simplified equations (4.23–4.24) may not be sufficient since they rely on the cancelling of the flow term in equation (4.18).

But we will first calculate the ion fraction, *as if* there is no flow in the formation region of Ne VIII.

To obtain the ion fraction, the same procedure is followed as with the other two ions. Ionisation states up to Ne IX is included; $n_{\text{Ne I}} + n_{\text{Ne II}} + ... + n_{\text{Ne IX}} = n_{\text{Ne}}$. The blue line in figure (4.11) upper panel shows the ion fraction of Ne VIII. The formation temperature is,

$$T^{form.}_{\text{Ne VIII}} \approx 6.2 \times 10^5 \text{K}$$

In the model by He et al. [2008] (figure 4.5 panel c) the formation temperatures for Ne VIII seem to be a approximately 8.0×10^5 K. A similar result has been found in the model 'F1' from Byhring et al. [2008] (8.6×10^5 K). A discrepancy between model values and $T^{form.}_{\text{Ne VIII}}$, calculated here, is expected because the outflow far from zero in this region. This may be interpreted as if the Ne VIII ions are carried out of ionisation equilibrium so that the maximum abundance of the ion is found at $\approx 8 \times 10^5$ K and not at $\approx 6.2 \times 10^5$ K. The red line in the upper panel show the line source region, which is located exactly at equilibrium formation temperature, $T^{form.}_{\text{Ne VIII}}$. Figure 4.11 lower panel shows time scales for Ne. Here we see that the ionisation time up to Ne VIII (solid red line), and recombination time from Ne VIII (dashed blue line) is actually shorter than the expansion time, a condition that suggests that Ne VIII *is* in ionisation equilibrium, which is unexpected. However, since the ratio of the expansion time scale to the ionisation time scale is only

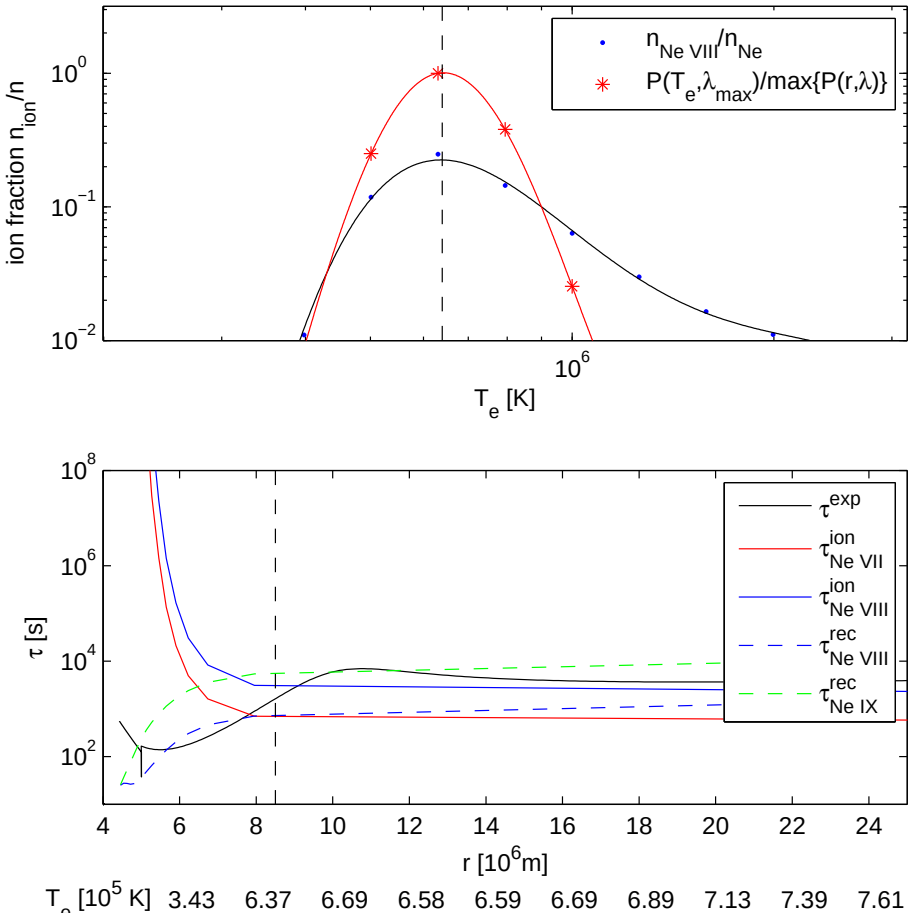

Figure 4.11: **Ne** VIII: Upper panel: Ionisation fraction and line source region of Ne VIII as a function of temperature. The vertical dashed black line is $T^{form.}_{\text{Ne VIII}}$. Lower panel: Time scales as a function of height. Here, the vertical dashed black line is $r^{form.}_{\text{Ne VIII}}$.

$\approx 10^{0.2} \approx 1.5$ times, it is questionable whether ionisation equilibrium really can be concluded only from this.

If $T^{form.}_{\text{Ne VIII}}$ given above would really be the formation temperature of this ion, then the formation height according to He et al. [2008] would be $r^{form.}_{\text{Ne VIII}} = 8.5 \times 10^6$ m, a large disagreement with Tu et al. [2005] who found $r^{form.}_{\text{Ne VIII}} = 20.6 \times 10^6$ m.

So the two models (He et al. [2008] vs. Byhring et al. [2008]) agree about the formation temperature of Ne VIII. But it should also be investigated whether the model by He et al. [2008] is able to predict the velocity correctly where Ne VIII is formed. We assume for a while that the observations are correct; Ne VIII is formed at 24×10^6 m (although Tu et al. [2005] on which the model by He is based found 20.6×10^6 m). And the Doppler velocity is, according to Tu et al. [2005], $9.6 \pm 2 \times 10^3$ ms^{-1}. Figure 4.5 panel b show that the outflow velocity agree with observations: $u \approx 8 \times 10^3$ ms^{-1} at $r = 24 \times 10^6$ m. In the model by Byhring et al. [2008], where the fraction of Ne VIII is also calculated, the equivalent velocity at $r = 24 \times 10^6$ m is $u \approx 16.7 \times 10^3$ ms^{-1} for the 'F1' funnel model and $u \approx 10.0 \times 10^3$ ms^{-1} for the 'F2' funnel model.

This shows first of all that the two models *do not* agree about outflow velocity in the formation region of Ne VIII. He et al. [2008] generally predict lower outflow velocity than any of the two funnel models of Byhring et al. [2008]. Secondly, what model that predicts the outflow velocity in best way really depends of what observational data to trust the most. Byhring et al. [2008] have used several sources of observational data, e.g. Wilhelm et al. [1998] and Dammasch et al. [1999] (and more) in addition to Tu et al. [2005], and have therefore assumed a larger error margin for the outflow of Ne VIII ($7 - 20 \times 10^3$ m^{-1} compared to $\pm 2 \times 10^3$ ms^{-1}). Thus both Byhring et al. [2008] and He et al. [2008] have found their result to be within observational constraints. Thirdly, different interpretation of observations may in some cases lead to differences. For example, the already mentioned difference 20.6 and 24×10^6 ms^{-1} may come from the fact that He et al. [2008] have read the formation height off to the right of maximum on the correlation plot, and not just off the maximum as Tu et al. [2005] have done.

The above evaluation shows that the model reproduces the observed red and blue shifts more or less correctly. In the following we will briefly discuss the major points of the model that are not addressed in the paper by He et al. [2008], but should be evaluated before this kind of model is accepted.

4.3.5 Points Not Addressed in the He et al. [2008] model

Even though the He et al. [2008] model fits the observed velocity constraints relatively well, there are several important points that are not considered in the paper but that can be expected to have a major impact on the model.

1. Generally it can not be assumed that heavy ions flow with the same speed as the protons (e.g. Lie-Svendsen and Esser [2005]) and should therefore be modelled in addition to the protons.

2. In the He et al. [2008] model the particles in the reconnecting loop are well mixed containing just the right amount of heavy ions. It is generally a problem to get heavy ions out of the chromosphere because gravitational forces may be significant here (Killie and Lie-Svendsen [2007]) This is a problem for both open and closed field regions. So even if the reconnection models are able to explain the observed red and blue shifts, the problem of getting the heavy ions into the loops still remains.

3. Which physical mechanism that determines the reconnection height of which the radial flow speed is exactly $u = 0$ is an issue that has not been addressed sufficiently. Fisk [2003] points out that the height of the loop is related to the temperature inside the loop, but the reconnection height is a more difficult parameter to predict. In He et al. [2008] it is also assumed that 1/2 of the mass flows down and the other 1/2 flows up, but an explanation to why this is exactly so is not given

Chapter 5

Summary and Discussion

In this work we have given an overview over how the idea of coronal funnels has developed. This idea originated from modelling and observations of the lower solar atmosphere. There have not been many solar wind models that have included such geometry. We have presented a few examples of such models which all seem to indicate that the model results are in better agreement with the observations compared to models that use more 'traditional' flow tube geometries (with smaller expansion). For example, Byhring et al. [2008] find that the ideal value of the outer funnel expansion is $f_{m2} = 4$, while Esser et al. [2005] arrive at $f_{m2} = 7$ as the most suitable expansion factor. Janse et al. [2007] reveal that the inclusion of helium in the funnel expansion leads to a new effect, namely two co-existing solutions; one slow and one fast wind solution that result from the same heating parameters. All the models mentioned here agree that the funnel geometry provides results that match observations in the best way.

We have then presented and studied in more detail a funnel model which is based on the ideas developed by Fisk [2003]. The only model of that kind that we could find in the literature that actually calculated such a model is the paper by He et al. [2008]. They have presented their model in order to explain the measured blue and red shift, but they do not actually calculate these lines or shifts. We have tried to evaluate the shifts in more detail to see whether the claim is justified. We have found that the model approximately predicts the measured Doppler shifts for all ions, including the large positive shift for Ne VIII and the slightly negative shift for Si II.

This model is relatively new, and it omits several important physical considerations, such as those mentioned in section 4.3.5: The ions should

be modelled separately since the velocity of the heavy ions and the lighter protons is generally not the same. And He et al. [2008] do not explain *why* the mass input occur at exactly $r = 5 \times 10^6$ m, nor how the heavy ions can possibly be well mixed with the lighter protons at this height.

But in general, the results of the model by He et al. [2008] agrees well with observations, for all the plasma parameters. And the equilibrium ion fractions and line source region calculated in this work are in agreement with results in other papers such as Byhring et al. [2008] for the regions with near zero velocity.

Bibliography

V. Abramenko, V. Yurchyshyn, and H. Watanabe. Parameters of the Magnetic Flux inside Coronal Holes. *ArXiv e-prints*, August 2009.

T. Aiouaz. Evidence of Relentless Reconnections at Boundaries of Supergranular Network Lanes in Quiet Sun and Coronal Hole. *The Astrophysical Journal*, 674:1144–1152, February 2008. doi: 10.1086/524029.

R. G. Athay. Responses of transition region models to magnetic field geometry and downflow velocities. *The Astrophysical Journal*, 263:982–986, December 1982. doi: 10.1086/160565.

W. M. Burton, C. Jordan, A. Ridgeley, and R. Wilson. The Structure of the Chromosphere-Corona Transition Region from Limb and Disk Intensities. *Royal Society of London Philosophical Transactions Series A*, 270:81–98, July 1971.

H. S. Byhring, R. Esser, and Ø. Lie-Svendsen. The Funnel Geometry of Open Flux Tubes in the Low Solar Corona Constrained by O VI and Ne VIII Outflow. *The Astrophysical Journall*, 673:L91–L94, January 2008. doi: 10.1086/527518.

Tina Christensen. *Energetic Electron Precipitation Studied by Atmospheric X-Rays (PhD thesis)*, pages 8–9. Niels Bohr Institute for Astronomy, Physics and Geophysics, 2002.

S. R. Cranmer et al. An Empirical Model of a Polar Coronal Hole at Solar Minimum. *The Astrophysical Journal*, 511:481–501, January 1999. doi: 10.1086/306675.

I. E. Dammasch, D. M. Hassler, W. Curdt, and K. Wilhelm. Statistical analysis of euv and uv lines inside and outside of solar coronal holes. *Space Science Reviews*, 87:161, 1999.

J. F. Dowdy, Jr., D. Rabin, and R. L. Moore. On the magnetic structure of the quiet transition region. *Solar Physics*, 105:35–45, May 1986. doi: 10.1007/BF00156374.

R. Esser and R. J. Edgar. Differential Flow Speeds of Ions of the Same Element: Effects on Solar Wind Ionization Fractions. *The Astrophysical Journal*, 563:1055–1062, December 2001. doi: 10.1086/323987.

R. Esser, Ø. Lie-Svendsen, Å. M. Janse, and M. A. Killie. Solar Wind from Coronal Funnels and Transition Region Lyα. *The Astrophysical Journall*, 629:L61–L64, August 2005. doi: 10.1086/444497.

L. A. Fisk. Acceleration of the solar wind as a result of the reconnection of open magnetic flux with coronal loops. *Journal of Geophysical Research (Space Physics)*, 108:1157–+, April 2003. doi: 10.1029/2002JA009284.

L. A. Fisk. The Open Magnetic Flux of the Sun. I. Transport by Reconnections with Coronal Loops. *The Astrophysical Journal*, 626:563–573, June 2005. doi: 10.1086/429957.

L. A. Fisk, N. A. Schwadron, and T. H. Zurbuchen. Acceleration of the fast solar wind by the emergence of new magnetic flux. *Journal of Geophysical Research*, 104:19765–19772, September 1999. doi: 10.1029/1999JA900256.

A. H. Gabriel. A magnetic model of the solar transition region. *Royal Society of London Philosophical Transactions Series A*, 281:339–352, May 1976.

P. Hackenberg, E. Marsch, and G. Mann. On the origin of the fast solar wind in polar coronal funnels. *Astronomy and Astrophysics*, 360:1139–1147, August 2000.

J.-S. He, C.-Y. Tu, and E. Marsch. Modeling of Solar Wind in the Coronal Funnel with Mass and Energy Supplied at 5 Mm. *Solar Physics*, 250: 147–158, July 2008. doi: 10.1007/s11207-008-9214-8.

Å. M. Janse, Ø. Lie-Svendsen, and E. Leer. Solar wind originating in funnels: fast or slow? *Astronomy and Astrophysics*, 474:997–1013, November 2007. doi: 10.1051/0004-6361:20066311.

M. A. Killie and Ø. Lie-Svendsen. Modeling Minor Ion Abundances in Quiescent Coronal Loops. *Astrophysical Journal*, 666:501–515, September 2007. doi: 10.1086/519437.

R.A. Kopp and T.E. Holzer. Dynamics of coronal hole regions, steady polytropic flows with multiple critical points. *Solar Physics*, 49:43, 1976.

Ø. Lie-Svendsen. The solar wind. In S. S. Hasan and D. Banerjee, editors, *Kodai School on Solar Physics*, volume 919 of *American Institute of Physics Conference Series*, pages 245–274, July 2007. doi: 10.1063/1.2756789.

Ø. Lie-Svendsen and R. Esser. Modeling the Energy Budget of Solar Wind Minor Ions: Implications for Temperatures and Abundances. *The Astrophysical Journal*, 618:1057–1073, January 2005. doi: 10.1086/426073.

P. Mazzotta, G. Mazzitelli, S. Colafrancesco, and N. Vittorio. Ionization balance for optically thin plasmas: Rate coefficients for all atoms and ions of the elements H to NI. *Astronomy and Astrophysics Supplement Series*, 133:403–409, December 1998.

M. P. Miralles, S. R. Cranmer, and J. L. Kohl. Low-latitude coronal holes during solar maximum. *Advances in Space Research*, 33:696–700, 2004. doi: 10.1016/S0273-1177(03)00239-4.

S. R. Pottasch. The Lower Solar Corona: Interpretation of the Ultraviolet Spectrum. *The Astrophysical Journal*, 137:945–+, April 1963. doi: 10.1086/147569.

R. Rosner, W. H. Tucker, and G. S. Vaiana. Dynamics of the quiescent solar corona. *The Astrophysical Journal*, 220:643–645, March 1978. doi: 10.1086/155949.

C.-Y. Tu and E. Marsch. Two-Fluid Model for Heating of the Solar Corona and Acceleration of the Solar Wind by High-Frequency Alfven Waves. *Solar Physics*, 171:363–391, April 1997.

C-Y. Tu et al. Solar wind origin in coronal funnels. *Science*, 308:519, 2005.

H. van Regemorter. Rate of Collisional Excitation in Stellar Atmospheres. *The Astrophysical Journal*, 136:906–+, November 1962. doi: 10.1086/147445.

J. E. Vernazza, E. H. Avrett, and R. Loeser. Structure of the solar chromosphere. III - Models of the EUV brightness components of the quiet-sun. *The Astrophysical Journals*, 45:635–725, April 1981. doi: 10.1086/190731.

K. Wilhelm et al. The Solar Corona above Polar Coronal Holes as Seen by SUMER on SOHO. *The Astrophysical Journal*, 500:1023–1038, June 1998. doi: 10.1086/305756.